

A SEARCH FOR OH MEGAMASERS AT $Z > 0.1$. III. THE COMPLETE SURVEY

JEREMY DARLING & RICCARDO GIOVANELLI

Department of Astronomy and National Astronomy and Ionosphere Center, Cornell University, Ithaca, NY
14853; darling@astro.cornell.edu; riccardo@astro.cornell.edu

Submitted to the Astronomical Journal, 6 December 2001; accepted 10 April 2002.

ABSTRACT

We present the final results from the Arecibo Observatory OH megamaser survey. We discuss in detail the properties of the remaining 18 OH megamasers detected in the survey, including 3 redetections. We place upper limits on the OH emission from 85 nondetections and examine the properties of 25 ambiguous cases for which the presence or absence of OH emission could not be determined. The complete survey has discovered 50 new OH megamasers (OHMs) in (ultra)luminous infrared galaxies ([U]LIRGs) which doubles the sample of known OHMs and increases the sample at $z > 0.1$ sevenfold. The Arecibo OH megamaser survey indicates that the OHM fraction in LIRGs is an increasing function of the far-IR luminosity (L_{FIR}) and far-IR color, reaching a fraction of roughly one third in the warmest ULIRGs. Significant relationships between OHMs and their hosts are few, primarily due to a mismatch in size scales of measured properties and an intrinsic scatter in OHM properties roughly equal to the span of the dataset. We investigate relationships between OHMs and their hosts with a variety of statistical tools including survival analysis, partial correlation coefficients, and a principal component analysis. There is no apparent OH megamaser “fundamental plane.” We compile data on all previously known OHMs and evaluate the possible mechanisms and relationships responsible for OHM production in merging systems. The OH-FIR relationship is reexamined using the doubled OHM sample and found to be significantly flatter than previously thought: $L_{OH} \propto L_{FIR}^{1.2 \pm 0.1}$. This near-linear dependence suggests a mixture of saturated and unsaturated masers, either within individual galaxies or across the sample.

Subject headings: masers — galaxies: interactions — galaxies: evolution — radio lines: galaxies — infrared: galaxies — galaxies: nuclei

1. INTRODUCTION

We have used the Arecibo telescope¹ to conduct a carefully designed OH megamaser (OHM) survey with the primary purpose of building the foundation required to employ OHMs as tracers of major galaxy mergers, dust-obscured starburst nuclei, and the formation of binary supermassive black holes spanning the epoch of galaxy evolution. Results of the survey have been presented in installments in Darling & Giovanelli (2000; hereafter Paper I) and Darling & Giovanelli (2001; hereafter Paper II). A detailed presentation of the survey selection criteria is given in Paper I. Papers I and II presented 35 OHMs, one OH absorber, and 160 nondetections, accounting for two-thirds of the survey. Here we present the remaining candidates, including 18 OHMs (14 new detections, three redetections, and one new OHM which falls outside of the survey parameter space), one OH absorber, 85 nondetections, and 25 ambiguous cases, and we summarize the results of the entire survey which doubles the sample of known OHMs and produces a sevenfold increase in those at $z > 0.1$.

Darling & Giovanelli (2002a; hereafter Paper IV) present the derivation of an OHM luminosity function and predicts the detectability and areal abundance of OHMs as a function of redshift for a number of galaxy merger evolution scenarios. Darling & Giovanelli (2002b; hereafter Paper V) present optical spectroscopy of OHM hosts and a study of OHM environments, lifetimes, and engines.

This paper (Paper III) is dedicated to releasing the remainder of the new OH megamaser detections in the complete Arecibo survey. We review the candidate selec-

tion method in §2 and the observation and data reduction methods in §3. Section 4 presents the results of the survey including an estimate of the completeness of OHM detections in the survey sample. We present a compilation of the OHMs known prior to the Arecibo survey, investigate the types of merging systems most likely to produce OHMs, and analyze the relationships between OHMs and their hosts in §5.

This study parameterizes the Hubble constant as $H_0 = 75 h_{75} \text{ km s}^{-1} \text{ Mpc}^{-1}$, assumes $q_0 = 0$, and uses $D_L = (v_{CMB}/H_0)(1 + 0.5 z_{CMB})$ to compute luminosity distances from v_{CMB} , the radial velocity of a radiation source in the cosmic microwave background (CMB) rest frame. Line luminosities are always computed under the assumption of isotropic emission.

2. CANDIDATE SELECTION

For the Arecibo OH megamaser survey, candidates were selected from the Point Source Catalog redshift survey (PSCz; Saunders *et al.* 2000), supplemented by the NASA/IPAC Extragalactic Database². The PSCz catalog is a flux-limited ($IRAS f_{60\mu m} > 0.6 \text{ Jy}$) redshift survey of 15,000 *IRAS* galaxies over 84% of the sky (see Saunders *et al.* 2000). We select *IRAS* sources which are in the Arecibo sky ($0^\circ < \delta < 37^\circ$), were detected at $60 \mu m$, and have $0.1 \leq z \leq 0.45$. The lower redshift bound is set to avoid local radio frequency interference (RFI), while the upper bound is set by the bandpass of the wide L-band receiver at Arecibo, although an effective upper bound is imposed around $z = 0.23$ by the RFI environment, as dis-

¹ The Arecibo Observatory is part of the National Astronomy and Ionosphere Center, which is operated by Cornell University under a cooperative agreement with the National Science Foundation.

² The NASA/IPAC Extragalactic Database (NED) is operated by the Jet Propulsion Laboratory, California Institute of Technology, under contract with the National Aeronautics and Space Administration.

cussed in §4.2. No constraints are placed on far-infrared (FIR) colors or luminosity. The redshift requirement limits the number of candidates in the Arecibo sky to 311. The condition that candidates have $z > 0.1$ automatically selects (ultra)luminous infrared galaxies ([U]LIRGs) if they are included in the PSCz. The strong influence of L_{FIR} and FIR color on OHM fraction in LIRGs is the primary reason for our high detection rate compared to previous surveys (e.g. Staveley-Smith *et al.* 1992; Baan, Haschick, & Henkel 1992). Baan (1991), Staveley-Smith *et al.* (1992), Baan, Haschick, & Henkel (1992), and others have noted the dependence of OHM fraction on the FIR luminosity and color, and these relationships are reexamined in §5.3.

3. OBSERVATIONS AND DATA REDUCTION

The upgraded Arecibo radio telescope offers new opportunities for the detection of OHMs, due to its improved sensitivity, frequency agility, and instantaneous spectral coverage. Its large collecting area makes it ideal for a survey of spectral lines at the upper end of the redshift range of the known OHM sample ($0.1 \leq z \leq 0.3$). Detection of OH emission lines is generally possible in a 4-minute integration, even at $z \simeq 0.2$. In roughly 200 hours of telescope time, we were able to observe about 300 OHM candidates and double the sample of known OHMs.

As described in Paper II, observations at Arecibo with the L-band receiver were performed by nodding on- and off-source, each for a 4 minute total integration, followed by firing a noise diode. Spectra were recorded in 1 s intervals to facilitate radio frequency interference flagging and excision in the time-frequency domain. Note that early observations reported in Paper I were sampled only every 6 s. Data were recorded with 9-level sampling in 2 polarizations of 1024 channels each, spanning a 25 MHz bandpass centered on redshifted 1666.3804 MHz (the mean of the 1667.359 and 1665.4018 MHz OH lines).

All reduction and analysis of these fast-sampled data was performed with the AIPS++ software package³ using home-grown routines for single dish reduction which are described in detail in Paper II. We included in the reduction pipeline RFI flagging routines designed to identify two types of RFI observed at Arecibo: strong features more than 3σ above the time-domain noise and spectrally broad, low-level RFI which is time-variable. A reliable estimate of the weight, or effective integration time, on a single channel is the total number of records used in forming the time average, excluding flagged records. Each spectral channel in a calibrated time-averaged spectrum may have a different effective integration time and hence a different effective intrinsic radiometer noise level. We include a normalized weights spectrum with each OHM spectrum in Figure 1. Depressions in the weights spectra indicate the presence of RFI, which may or may not have been completely flagged and removed from the final spectra. Spectral channels with low weights should thus be treated with skepticism. The frequency resolution after hanning smoothing is 49 kHz (10 km s^{-1} at $z = 0.1$), and

³ The AIPS++ (Astronomical Information Processing System) is a product of the AIPS++ Consortium. AIPS++ is freely available for use under the Gnu Public License. Further information may be obtained from <http://aips2.nrao.edu>.

the uncertainty in the absolute flux scale is 8%.

4. SURVEY RESULTS

The survey selection criteria identify 312 candidate OHMs in the PSCz. One of these, *IRAS* 10232+1258, has an incorrect redshift in the catalog, and the correct redshift places it below the $z > 0.1$ selection threshold ($z = 0.0325$; Haynes *et al.* 1997). Hence, of the 311 remaining candidates, 52 are OHMs (3 were previously identified; 15 are new detections reported in this paper), 1 is an OH absorber (reported here), 233 do not show OH emission lines down to the detection threshold (85 of these are reported in this paper), and 25 remain ambiguous (reported here) mostly due to anthropogenic RFI and Galactic HI “RFI.” The latter appears at $z = 0.174$ (1420 MHz), where strong Galactic HI emission interferes with the detection of comparatively weak OH lines. Overall, we find one OH megamaser in every 5.5 candidates. Further discussion of the OHM fraction in mergers is presented in §5. Three objects deserve special mention: *IRAS* F13451+1232 has a tentative OH detection (Dickey *et al.* 1990), but could not be confirmed in this survey due to its strong radio continuum (see §4.2) and is listed with the ambiguous candidates (it is not included in detection statistics and is not counted as an OHM in the survey); *IRAS* F11180+1623 is not included in the PSCz sample, but is a new OHM detection and is listed in the OH detection tables and spectra but is not included in the survey statistics and analysis; and *IRAS* F19154+2704 is not included in the PSCz sample, but is a new OH absorber listed in Paper I which is not included in the survey statistics and analysis.

4.1. Nondetections

Tables 1 and 2 list respectively the optical/FIR and radio properties of the 85 OH non-detections in the last third of the survey. Table 1 lists the optical redshifts and FIR properties of the non-detections in the following format: Column (1) lists the *IRAS* Faint Source Catalog (FSC) name. Columns (2) and (3) list the source coordinates (epoch B1950.0) from the FSC, or the Point Source Catalog (PSC) if unavailable in the FSC. Columns (4), (5) and (6) list the heliocentric optical redshift, reference, and corresponding velocity. Uncertainties in velocities are listed whenever they are available. Column (7) lists the cosmic microwave background rest-frame velocity. This is computed from the heliocentric velocity using the solar motion with respect to the CMB measured by Lineweaver *et al.* (1996): $v_{\odot} = 368.7 \pm 2.5 \text{ km s}^{-1}$ towards $(l, b) = (264^{\circ}31 \pm 0^{\circ}16, 48^{\circ}05 \pm 0^{\circ}09)$. Column (8) lists the luminosity distance computed from v_{CMB} via $D_L = (v_{CMB}/H_0)(1 + 0.5z_{CMB})$, assuming $q_0 = 0$. Columns (9) and (10) list the *IRAS* 60 and 100 μm flux densities in Jy. FSC flux densities are listed whenever they are available. Otherwise, PSC flux densities are used. Uncertainties refer to the last digits of each measure, and upper limits on 100 μm flux densities are indicated by a “less-than” symbol. Column (11) lists the logarithm of the far-infrared luminosity in units of $h_{75}^{-2} L_{\odot}$. L_{FIR} is computed following the prescription of Fullmer & Lonsdale (1989): $L_{FIR} = 3.96 \times 10^5 D_L^2 (2.58f_{60} + f_{100})$, where f_{60} and f_{100} are the 60 and 100 μm flux densities expressed in Jy, D_L is in h_{75}^{-1} Mpc, and L_{FIR} is in units of $h_{75}^{-2} L_{\odot}$.

If f_{100} is only available as an upper limit, the permitted range of L_{FIR} is listed. The lower bound on L_{FIR} is computed for $f_{100} = 0$ Jy, and the upper bound is computed with f_{100} set equal to its upper limit. The uncertainties in D_L and in the *IRAS* flux densities typically produce an uncertainty in $\log L_{FIR}$ of 0.03.

Table 2 lists the 1.4 GHz flux density and the limits on OH emission of the non-detections in the following format: Column (1) lists the *IRAS* FSC name, as in Table 1. Column (2) lists the heliocentric optical redshift, as in Table 1. Column (3) lists $\log L_{FIR}$, as in Table 1. Column (4) lists the predicted isotropic OH line luminosity, $\log L_{OH}^{pred}$, based on the Malmquist bias-corrected L_{OH} - L_{FIR} relation determined by Kandalian (1996) from 49 OHMs: $\log L_{OH} = (1.38 \pm 0.14) \log L_{FIR} - (14.02 \pm 1.66)$ (see §5.4). Column (5) lists the upper limit on the isotropic OH line luminosity, $\log L_{OH}^{max}$. The upper limits on L_{OH} are computed from the RMS noise of the non-detection spectrum assuming a “boxcar” line profile of rest frame width $\Delta v = 150 \text{ km s}^{-1}$ and height 1.5σ :

$$L_{OH}^{max} = 4\pi D_L^2 1.5\sigma \left(\frac{\Delta v}{c} \right) \left(\frac{\nu_o}{1+z} \right). \quad (1)$$

The assumed rest frame width $\Delta v = 150 \text{ km s}^{-1}$ is the average FWHM of the 1667 MHz line of the known OHM sample. Column (6) lists the on-source integration time, in minutes. Column (7) lists the RMS noise values in flat regions of the non-detection baselines, in mJy, after spectra were hanning smoothed to a spectral resolution of 49 kHz. Column (8) lists 1.4 GHz continuum fluxes, from the NRAO VLA Sky Survey (NVSS; Condon et al. 1998). If no continuum source lies within $30''$ of the *IRAS* coordinates, an upper limit of 5.0 mJy is listed. Column (9) lists the optical spectroscopic classification, if available. Codes used are: “S2” = Seyfert type 2; “S1” = Seyfert type 1; “H” = HII region (starburst); and “L” = low-ionization emission region (LINER). References for the classifications are listed in parentheses and included at the bottom of the Table. Column (10) lists source notes, which are given at the foot of the table.

We can predict the expected isotropic OH line luminosity, L_{OH}^{pred} , for the OHM candidates based on the L_{OH} - L_{FIR} relation determined by Kandalian (1996; see §5.4) and compare this figure to upper limits on the OH emission derived from observations, L_{OH}^{max} , for a rough measure of the confidence of the non-detections. Note, however, that the scatter in the L_{OH} - L_{FIR} relation is quite large: roughly half an order of magnitude in L_{FIR} and one order of magnitude in L_{OH} (see Kandalian 1996). Among the non-detections, 34 out of 233 galaxies have $L_{OH}^{pred} < L_{OH}^{max}$, indicating that longer integration times are needed to unambiguously confirm these non-detections, and 33 out of 233 candidates have L_{OH}^{max} within the range of L_{OH}^{pred} set by an upper limit on f_{100} . Integration times were a compromise between efficient use of telescope time and the requirement for a meaningful upper limit on L_{OH} for non-detections.

4.1.1. Notes on Nondetections

12514+1027: There are two redshifts for this object in the literature: 0.30 (Wilman *et al.* 1998) and 0.3189 (PSCz). We have coverage of both redshifts and find no

clear OH emission, but there are regions in the bandpass between the two frequencies which are unobservable due to RFI. We use the PSCz redshift as the fiducial for computing luminosities and limits on the OH emission of this object.

4.2. Ambiguous Candidates

Despite careful observations and RFI mitigation measures, there remain 25 OHM candidates in the survey for which no OH measurement could be made. One of these, *IRAS* 13451+1232, is likely to be an OHM (Dickey *et al.* 1990). There are two factors which frustrate weak spectral line observations: RFI and strong radio continuum in the beam.

RFI can be anthropogenic or Galactic HI which makes OH undetectable at velocities around 52000 km s^{-1} . The effect of RFI is to constrain the survey sample in redshift. A group of candidates near $z = 0.174$ is excluded from the sample by Galactic HI, and most candidates above $z = 0.23$ are not observable except in small RFI-free windows. The exclusion of candidates by the Galactic HI will not significantly bias the survey, but the irregular redshift coverage above $z = 0.23$ will produce a bias. The best solution to this bias would be to impose an upper cutoff in redshift for the survey.

Strong radio continuum sources (including the Sun) produce standing waves between the instrument platform and the primary reflector at Arecibo, making complicated baseline structures which obliterate the signatures of weak spectral lines. This may be a significant source of bias for the survey, because these IR quasars represent a special population which may become increasingly important at higher redshifts. However, there are only 4 strong continuum sources in the survey which are RFI-free, representing a small potential contribution to the overall survey statistics.

Tables 3 and 4 list, respectively, the optical/FIR and radio properties of the 25 ambiguous candidates. The column headings of Table 3 are identical to those of Table 1, except for the final column which lists notes describing the source of ambiguity for each object. Table 4 lists the 1.4 GHz flux density, the optical classification, and notes on each candidate in the following format: Column (1) lists the *IRAS* FSC name, as in Table 1. Column (2) lists the heliocentric optical redshift, as in Table 1. Column (3) lists $\log L_{FIR}$, as in Table 1. Column (4) lists the predicted isotropic OH line luminosity, $\log L_{OH}^{pred}$, based on the Malmquist bias-corrected L_{OH} - L_{FIR} relation determined by Kandalian (1996; see §5.4). Column (5) lists 1.4 GHz continuum fluxes from the NVSS. If no continuum source lies within $30''$ of the *IRAS* coordinates, an upper limit of 5.0 mJy is listed. Column (6) lists the optical spectroscopic classification, if available: (S1) Seyfert type 1, (S2) Seyfert type 2, (Q) Quasar, and (L) low-ionization emission region (LINER). References for the classifications are shown in parentheses and included at the foot of the table. Column (7) lists source notes, which are given at the foot of the table.

4.2.1. Notes on Ambiguous Detections

13451+1232: We attempted to make a re-observation of this tentative OH detection by Dickey *et al.* (1990), but the

strong radio continuum (5.4 Jy) produced standing waves in the spectrum and frustrated detection of any OH lines. The host of this probable OHM is classified a Seyfert 2 by Kim, Veilleux, & Sanders (1998) and a Seyfert 1.5 by Baan, Salzer, & LeWinter (1998) (the latter indicate that two nuclei were observed, but only one classification is listed for this object). Veilleux, Sanders, & Kim (1997) have detected broad Pa α emission from this merger, indicating that it contains a buried quasar. In fact, many groups refer to this object as an “IR quasar”. This is a double nucleus system, with nuclear separation of 3'' (7.1 kpc) and ample molecular gas: $\log M(H_2) = 10.78$ (Scoville *et al.* 2000).

4.3. OH Megamaser Detections

Tables 5 and 6 list respectively the optical/FIR and radio properties of the 15 new OHM detections, the three redetections, and one OH absorber. Note that OHM IRAS F11180+1623 is *not* in the PSCz sample, but was observed along with other OHM candidates not found in the PSCz sample to fill in telescope time when local sidereal time coverage of the official sample was sparse. This detection is not included in any survey statistics or interpretation. Spectra of the 18 OHMs appear in Figure 1, and spectra of the OH absorber appears in Figure 2. The column headings of Table 5 are identical to those of Table 1. Table 6 lists the OH emission properties and 1.4 GHz flux density of the OH detections in the following format: Column (1) lists the IRAS FSC name. Column (2) lists the measured heliocentric velocity of the 1667.359 MHz line, defined by the center of the FWHM of the line. The uncertainty in the velocity of the line center is estimated assuming an uncertainty of ± 1 channel (± 49 kHz) on each side of the line. Although one can generally determine emission line centers with much higher precision when the shapes of lines are known, the OHM line profiles shown in Figure 1 are asymmetric, multi-component, and non-gaussian. They defy simple shape descriptions, so we use this conservative and basic prescription to quantify the uncertainty in the line centers. Column (3) lists the on-source integration time in minutes. Column (4) lists the peak flux density of the 1667 MHz OH line in mJy. Column (5) lists the equivalent width-like measure in MHz. W_{1667} is the ratio of the integrated 1667 MHz line flux to its peak flux. Ranges are listed for W_{1667} in cases where the identification of the 1665 MHz line is unclear, but in many cases the entire emission structure is included in W_{1667} as indicated in the discussion of each source below. Column (6) lists the observed FWHM of the 1667 MHz OH line in MHz. Column (7) lists the rest frame FWHM of the 1667 MHz OH line in km s^{-1} . The rest frame width was calculated from the observed width as $\Delta v_{rest} = c(1+z)(\Delta\nu_{obs}/\nu_o)$. Column (8) lists the hyperfine ratio, defined by $R_H = F_{1667}/F_{1665}$, where F_ν is the integrated flux density across the emission line centered on ν . $R_H = 1.8$ in thermodynamic equilibrium. In many cases, the 1665 MHz OH line is not apparent, or is blended into the 1667 MHz OH line, and a good measure of R_H becomes difficult without a model for the line profile. It is also not clear that the two lines should have similar profiles, particularly if the lines are aggregates of many emission regions in different saturation states. Some spectra allow a lower limit to be placed on R_H , indicated by a “greater than” symbol. Blended or noisy lines have uncertain values of R_H , and are indi-

cated by a tilde, but in some cases, separation of the two OH lines is impossible and no value is listed for R_H . Column (9) lists the logarithm of the FIR luminosity, as in Table 5. Column (10) lists the predicted OH luminosity, $\log L_{OH}^{pred}$, as in Table 2. Column (11) lists the logarithm of the measured isotropic OH line luminosity, which includes the integrated flux density of both the 1667.359 and the 1665.4018 MHz lines. Note that L_{OH}^{pred} is generally less than the actual L_{OH} detected (46 out of 53 detections). Column (12) lists the 1.4 GHz continuum fluxes from the NVSS. If no continuum source lies within 30'' of the IRAS coordinates, an upper limit of 5.0 mJy is listed.

The spectra of the OH detections are presented in Figures 1 and 2. The abscissae and inset redshifts refer to the optical heliocentric velocity, and the arrows indicate the expected velocity of the 1667.359 (*left*) and 1665.4018 (*right*) MHz lines based on the optical redshift, with error bars indicating the uncertainty in the redshift. The spectra refer to 1667.359 MHz as the rest frequency for the velocity scale. Spectra have had the dotted baselines subtracted, and the baselines have been shifted in absolute flux density such that the central channel has value zero. The small frame below each spectrum shows a weights spectrum, indicating the fractional number of records used to form the final spectrum after the RFI rejection procedure (see §3 and Paper II). Channels with weights close to unity are “good” channels, whereas channels with lower than average weight are influenced by time-variable RFI and are thus suspect. The weights spectra are presented to indicate confidence in various spectral features, but note that often the RFI rejection procedure does a good job of cleaning channels and that channels with $\sim 10\%$ rejected records may be completely reliable (this is, after all, the point of the RFI cleaning procedure).

In order to quantitatively identify dubious 1665 MHz OH line detections, we compute the autocorrelation function (ACF) of each spectrum and locate the secondary peak (the primary peak corresponds to zero offset, or perfect correlation). Any correspondence of features between the two main OH lines will enhance the second autocorrelation peak and allow us to unambiguously identify 1665 MHz lines based not strictly on spectral location and peak flux, but on line shape as well. The secondary peak in the ACF of each spectrum, when present, is indicated by a small solid line over the spectra in Figure 1. We expect the offset of the secondary peak to be equal to the separation of the two main OH lines, properly redshifted: $(1.9572 \text{ MHz})/(1+z)$. The *expected* location of the secondary ACF peak is indicated in Figure 1 by a small dashed line over each spectrum. Both the expected and actual secondary peak positions are plotted offset with respect to the center of the 1667 MHz line, as defined by the center of the FWHM, rather than the peak flux.

We examined the Digitized Sky Survey⁴ (DSS) images of each new OH detection. The OHM hosts are gener-

⁴ Based on photographic data obtained using Oschin Schmidt Telescope on Palomar Mountain. The Palomar Observatory Sky Survey was funded by the National Geographic Society. The Oschin Schmidt Telescope is operated by the California Institute of Technology and Palomar Observatory. The plates were processed into the present compressed digital format with their permission. The Digitized Sky Survey was produced at the Space Telescope Science Institute under U.S. Government grant NAG W-2166.

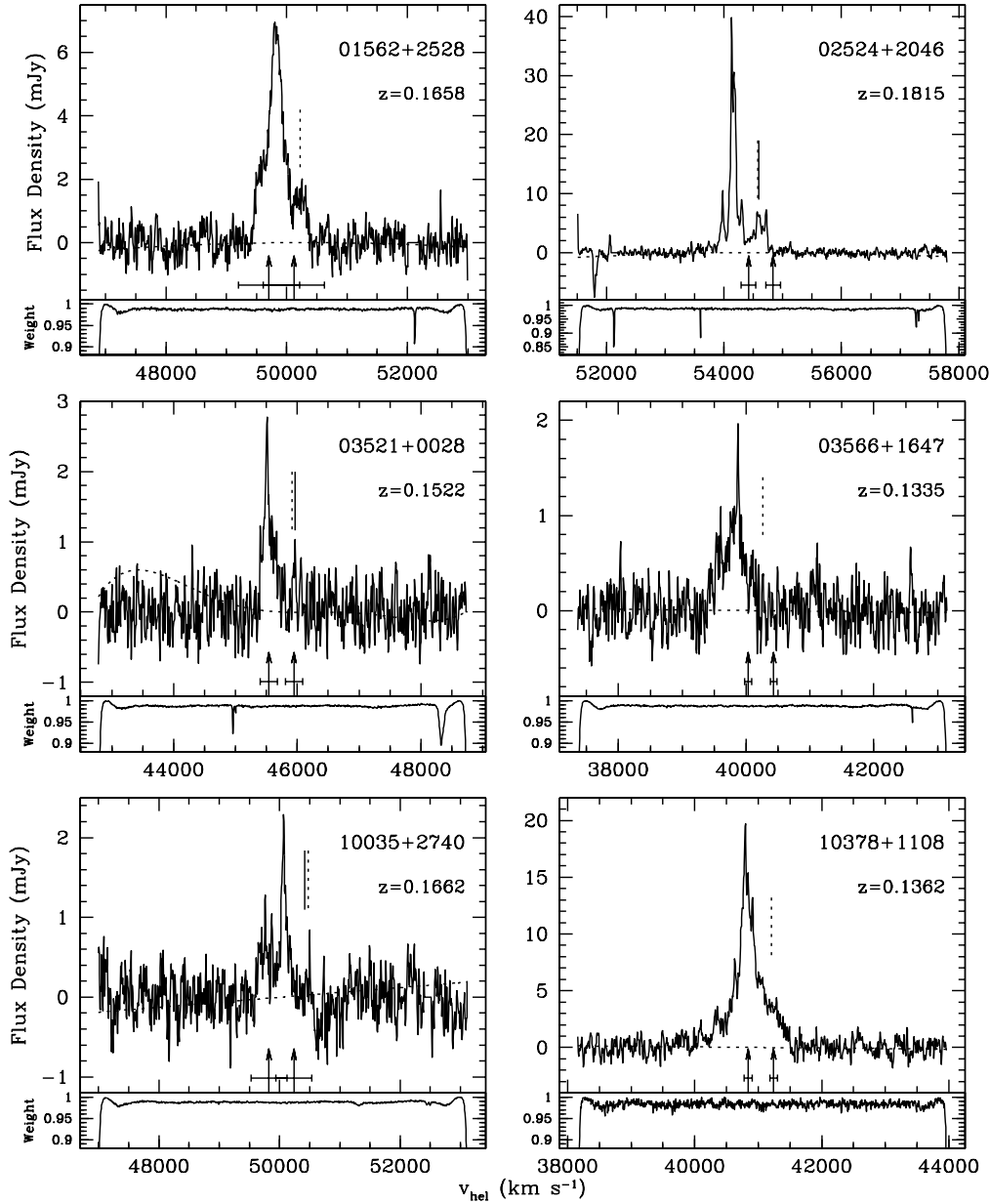


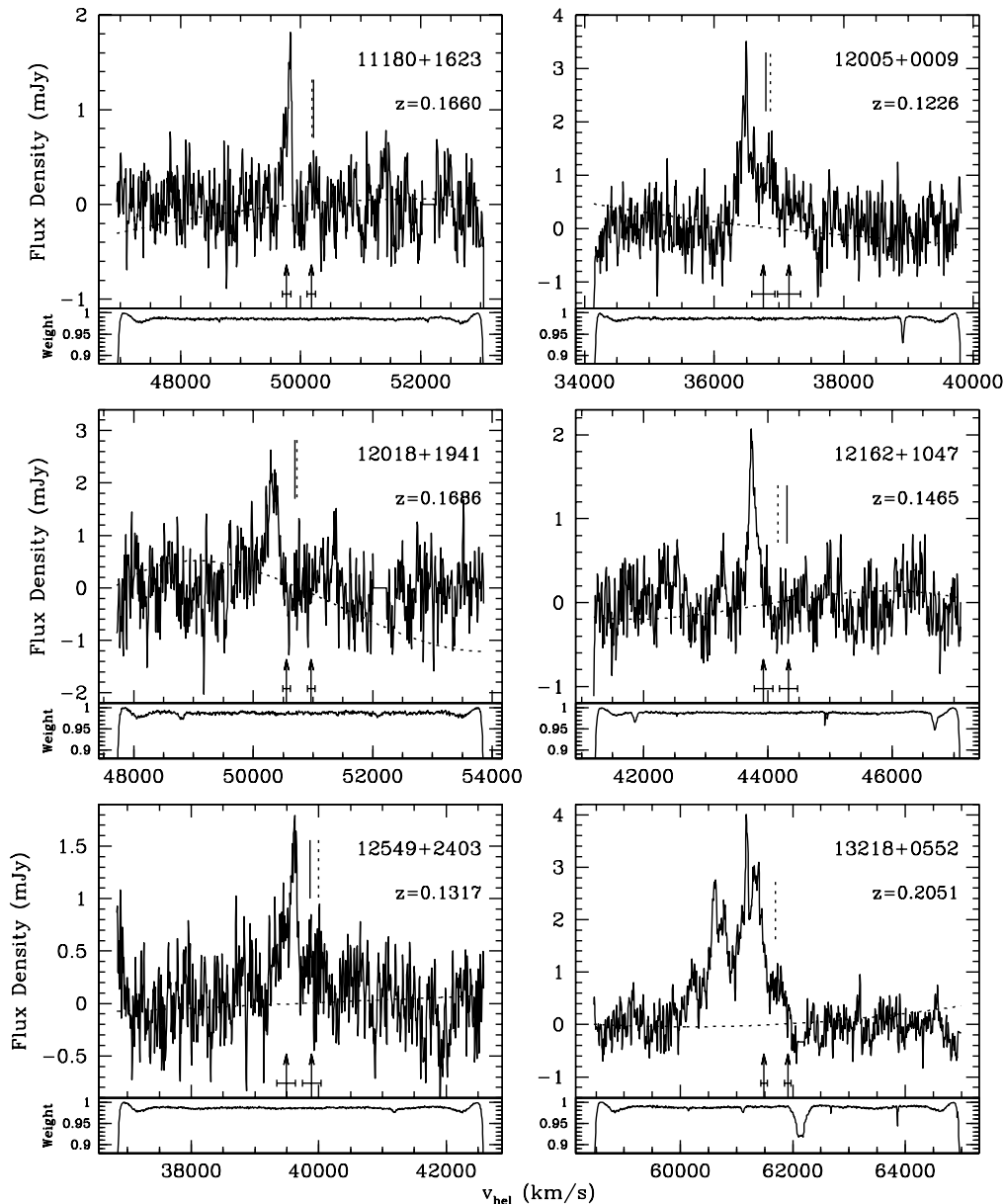
FIG. 1.— New OH megamasers discovered in (U)LIRGs. Abscissae and inset redshifts refer to the optical heliocentric velocity. Spectra use the 1667.359 MHz line as the rest frequency for the velocity scale. Arrows indicate the expected velocity of the 1667.359 (*left*) and 1665.4018 (*right*) MHz lines based on the optical redshift, with error bars indicating the uncertainty in the redshift. Solid vertical lines indicate the location of the secondary maximum in the autocorrelation function, and dashed vertical lines indicate the expected position of the 1665 MHz line, based on the centroid of the 1667 MHz line; a match between the two indicates a possible detection of the 1665 MHz line. The dotted baselines indicate the shape (but not the absolute magnitude) of the baselines subtracted from the calibrated spectra. The small frame below each spectrum shows the “weights” spectrum, indicating the fractional number of RFI-free records averaged in each channel. The properties of these megamasers are listed in Tables 5 and 6.

ally faint, unresolved, and unremarkable in the DSS unless otherwise noted in the discussion of individual sources below. We also performed an exhaustive literature search for each new OHM, and searched the Hubble Space Telescope (HST) archives for fields containing OHM hosts. All relevant data are included in the discussions below. The weights spectra are generally clean across the OH line profiles, unless specifically noted. Note that the sampling rate for the first OHM detections in the survey (Paper I) was too slow to perform the RFI cleaning procedure discussed in Paper II, so these OHMs do not have weights spectra available. Included in the discussion below are the opti-

cal spectral types of OHM hosts from the literature and from observations presented in Paper V. We make some observations and measurements specific to individual OH detections as follows.

4.3.1. Notes on OH Megamasers

01562+2528: This OHM shows broad, blended lines, which are easily identified, despite the highly uncertain optical redshift. Although the ACF shows no second peak, the 1665 MHz line is quite prominent. Galactic HI has been masked at 52200 km s⁻¹. The DSS image of the host of this OHM shows a multi-component object with

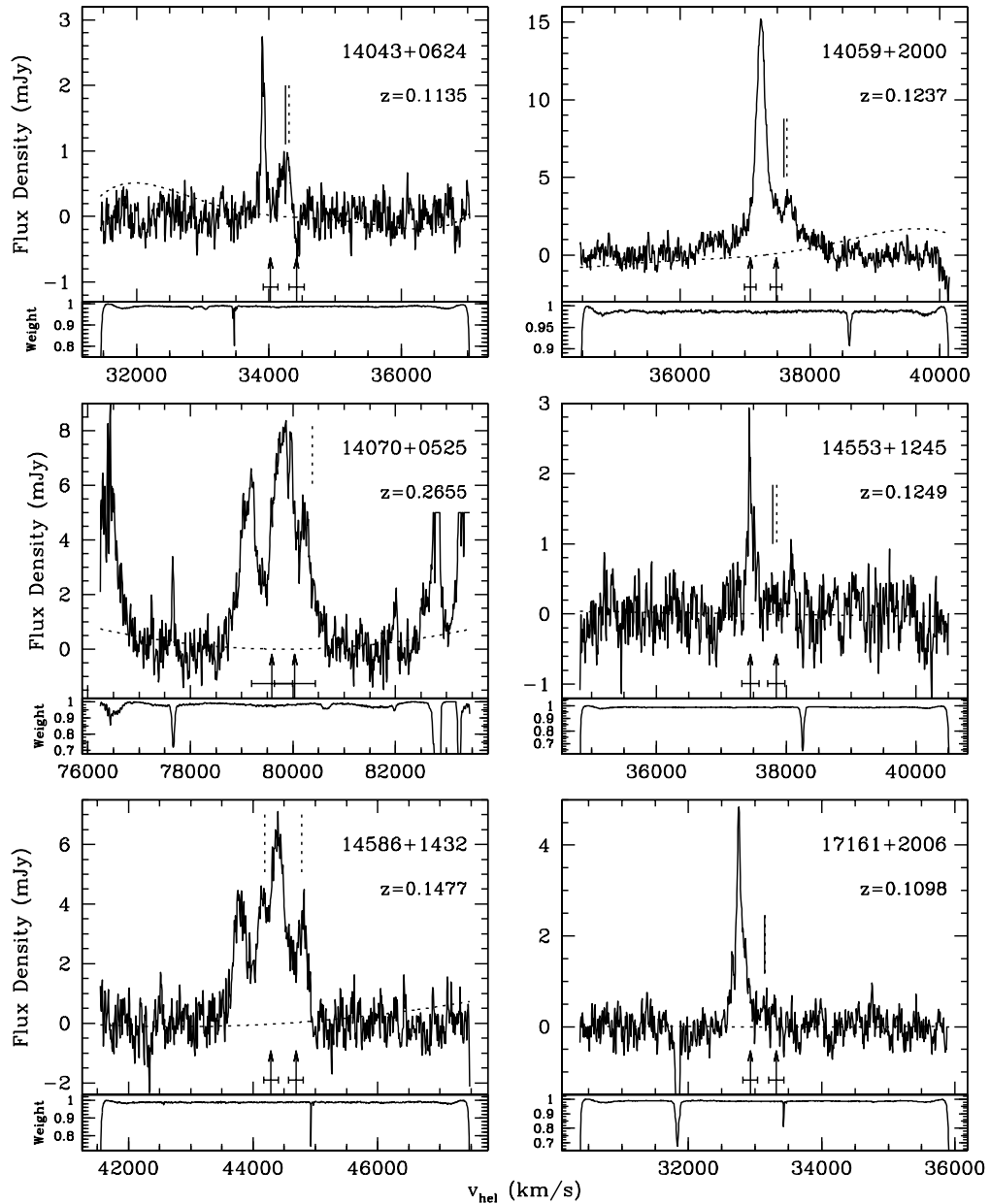
FIG. 1.— *continued.*

possible extended emission. Observations at the Palomar 5 m telescope confirm this with the detection of two nuclei (Paper V). We classify the northeast nucleus of this OHM host a starburst. The southwest nucleus lacked sufficient signal for optical classification, but a redshift was measured (see Paper V). The velocity of the NE nucleus is consistent with the OH redshift but the SW nucleus is not.

02524+2046: This OHM has the most unusual spectrum of the survey sample. The peak flux density is 40 mJy; RFI and receiver considerations aside, such an OHM would be detectable beyond $z = 1$ at Arecibo in a short integration time. The emission lines are strong, narrow, and show extremely good correspondence between 1667 and 1665 lines, including a blue tail on each complex. The correspondence is so good that we can measure the hyperfine ratio for each component of the line profile. From high velocity to low, we find $R_H = 1.40, 5.63, 1.88$ (Table 6 lists

the hyperfine ratio of the combined emission: $R_H = 3.2$). Galactic HI has been masked in the spectrum, and is accompanied by a dip in the weights spectrum. There is also an interesting feature at 51800 km s⁻¹ which is likely to be HI in the off-source position (5^m later than the on-source position) with a heliocentric velocity of about -300 km s⁻¹. This is probably associated with the Magellanic stream. We classify the host of this OHM a starburst (Paper V).

03521+0028: The optical redshift perfectly matches the 1667 MHz line as well as the marginally significant 1665 MHz line. The feature identified as the 1665 MHz line by the ACF and the position of the 1667 MHz line is a 3.4σ detection and is quite narrow. The host of this OHM is classified in the mid-IR as starburst by Lutz, Veilleux, & Genzel (1999) and in the optical as a LINER by Veilleux, Kim, & Sanders (1999) and us (Paper V). K-band imaging by Murphy *et al.* (1996) gives a nuclear separation of $1.6''$

FIG. 1.— *continued.*

or 3.6 kpc. Solomon *et al.* (1997) measure a CO(1–0) line width of 150 km s^{-1} , estimate a H_2 mass of $4.3 \times 10^{10} M_\odot$, and derive a blackbody radius of 319 pc.

03566+1647: There is no obvious 1665 MHz line in this OHM spectrum, and the ACF shows no secondary peak. We compute an upper limit on the 1665 MHz line flux assuming a 1σ line of width equal to the 1667 MHz line to obtain a lower limit on the hyperfine ratio: $R_H \gtrsim 9.6$. The optical redshift does not correspond to the peak OH emission. We classify the host of this OHM a Seyfert 2 (Paper V).

10035+2740: This OHM has a number of sharp lines, and it is unclear if the 1665 MHz line is present (there is a narrow 4σ line somewhat above the expected position which is included in the estimate of R_H). Galactic HI has been masked in the final spectrum. The spectrum is somewhat noisy, and it is unclear if the multiple peaks are

OH or noise; there are two broad lines and smaller spikes on the less prominent line. The weights spectrum is very clean.

10378+1108: This OHM is a re-detection, and was discovered by Kazes & Baan (1991). The measured properties listed in Table 6 are consistent with those measured by Kazes & Baan (1991), and the spectra are similar, but comparison is difficult due to very different signal to noise observations. The spectrum in Figure 1 shows a strong line with broad red and blue wings with no clear 1665 MHz line. The ACF of this spectrum shows no second peak. K-band imaging by Murphy *et al.* (1996) obtain an upper limit on the nuclear separation (if any) of this OHM host: $< 0.5''$ or $< 1.1 \text{ kpc}$. The host of this OHM is classified a LINER by Veilleux, Kim, & Sanders (1999) and by us (Paper V).

11180+1623: *Note that this object is NOT in the PSCz*

sample. The emission profile of this OHM has a sharp red falloff and a blue tail. The 1665 MHz line identified by the ACF and the 1667 MHz line prediction has 2.8σ significance, but resembles other baseline features. The hyperfine ratio measured from this line is thus treated as a lower limit. Galactic HI has been masked in the spectrum presented in Figure 1.

12005+0009: This OHM has at least three distinct emission components and a very broad total spectrum (1081 km s^{-1} in the rest frame at 10% of the peak flux density). The ACF is broad and multiply-peaked, but seems to indicate the secondary component as the 1665 MHz line, in agreement with the prediction from the center of the main 1667 MHz line. All components are included in the total OH measure, but we tentatively identify the secondary component as the 1665 MHz line for a rough measure of the hyperfine ratio which excludes the highest velocity tertiary component: $R_H \sim 2.0$. The DSS image of the OHM host is extended and irregular.

12018+1941: We redetect an OHM first observed by Martin *et al.* (1988). The spectra look similar and all of the measurements presented in Table 6 are consistent with those of Martin *et al.* (1988), but the uncertainties are high in both detections due to low signal to noise. Galactic HI has been masked in the spectrum presented in Figure 1. The ACF shows a minor second peak, although there is no significant spectral feature where we expect a 1665 MHz line. We compute a lower bound on R_H , assuming a 1σ 1665 MHz profile with width equal to the 1667 MHz line: $R_H \geq 5.6$. The host of this OHM is classified a LINER by Baan, Salzer, & LeWinter (1998) and by Veilleux, Kim, & Sanders (1999), although the latter group notes that it could be a Seyfert 2.

12162+1047: This OHM has no obvious 1665 MHz line, and mild standing waves in the baseline. We measure only the main line, since the smaller line on the blue side is similar in size and shape to noise features in the bandpass. The ACF has no significant second peak. Assuming a 1σ profile with width equal to the 1667 MHz line width, we obtain a rough upper bound on the 1665 MHz emission which provides a lower bound on the hyperfine ratio: $R_H \geq 11.1$. The DSS image shows a pair of overlapping galaxies with significant separation (roughly $11''$ or 26 kpc).

12549+2403: This OHM has a sharp, well-defined second peak in the ACF. The 1665 MHz line is poorly defined in the spectrum, and if present, has a 3.6σ peak. There are mild standing waves in the bandpass which could masquerade as the 1665 MHz line. The 1667 MHz line is asymmetrical, with sharp red falloff and a blue tail. The DSS image of this object is extended and elliptical in shape but more or less regular (no clear signs of interaction).

13218+0552: The host of this OHM is classified as a QSO or Seyfert 1 (Low *et al.* 1988), and is one of three Seyfert 1 hosts of OH megamasers. The other two are Mrk 231 (*IRAS* 12540+5708; Baan, Haschick, & Henkel 1992; Baan, Salzer, & LeWinter 1998; Kim, Veilleux, & Sanders 1998) and UGC 545 (*IRAS* 00509+1225; Bottinelli *et al.* 1990; Sanders *et al.* 1988), and Tables 7 and 8 list the properties of these OHMs. The OH spectrum of 13218+0552 shows two main broad emission peaks with a separation of 490 km s^{-1} in the rest frame which may be associated with multiple nuclei. The FWHM listed in Table 6 is measured

from the strongest line. The overall spectrum shows many significant peaks (at least 4) and is quite broad, spanning 1560 km s^{-1} in the rest frame at 10% of the peak flux density. Disentangling the 1665 and 1667 MHz lines is not possible in this spectrum, so W_{1667} is measured from the entire profile. Note that there are dips in the weights spectrum, two of which coincide with the OH spectrum. The small dip at 61100 km s^{-1} does not correspond to any OH peak or feature, indicating that this RFI was properly cleaned. The broad feature in the weights spectrum at 62200 km s^{-1} indicates the presence of a global positioning system downlink signal at 1381 MHz. This signal could not be completely removed from the OH spectrum and was masked in the final spectrum. Boyce *et al.* (1996) have imaged the host of this QSO with HST. The host shows tidal features and possibly a double nucleus with separation less than 1 kpc. Boyce *et al.* propose that while this object does not technically qualify as an optical QSO (only as a Seyfert 1), it contains a luminous buried QSO. Lo, Chen, & Ho (1999) obtain an upper bound on the H_2 mass of this object from CO(1–0) observations at the NRAO 12 m antenna: $M(H_2) < 2.4 \times 10^{10} M_\odot$.

14043+0624: This OHM has a well-defined but broad 1665 MHz line. There is an absorption feature at the edge of the 1665 MHz line which is not identified as RFI by the weights spectrum. If it is RFI which is stable in time or low-level, then it will not be identified and removed by the RFI flagging routine, and may also affect the 1665 MHz line. This would explain the unusually broad and strong 1665 MHz line which produces an anomalous hyperfine ratio below the thermodynamic equilibrium value: $R_H = 1.4$. The depression in the weights spectrum at 33450 km s^{-1} marks locally generated RFI at 1500 MHz.

14059+2000: The spectrum of this OHM has a few low-level features which may or may not be OH emission. This spectrum has a strong main peak, a significant 1665 MHz line, and broad wings, especially on the red side. The width at 10% of the peak flux density is surprising: 1650 km s^{-1} in the rest frame. The 1667 MHz line measurements exclude the red wing and the broad low-level blue emission feature, but all components are included in the total OH measurement. L_{OH} is more than an order of magnitude larger in this OHM than L_{OH}^{pred} .

14070+0525: This is an OH gigamaser, and the most distant OHM known at $z = 0.2655$. It was discovered by Baan *et al.* (1992), and redetected in this survey. The OH lines fall nicely into a clean spectral window, and the spectrum illustrates the difficulty of OH spectral line observations beyond $z \simeq 0.2$. The RFI has been truncated on the high velocity side of the spectrum. The weights spectrum clearly identifies the RFI seen in the spectrum, but the cleaning procedure does not remove all of the RFI because it is present in every record. Note that the weights spectrum is clean across the OH spectrum. The OH lines are broad and blended, and identification of a 1665 MHz line is not possible. The multiple broad peaks suggest multiple masing nuclei in this object. The FWHM quoted in Table 6 is measured from the strongest component. The width at 10% of peak flux density is 1580 km s^{-1} in the rest frame. A comparison of the spectrum in Figure 1 and the spectrum in Baan *et al.* (1992) shows no significant spectral profile changes, although the flux calibration seems

to be different between the two: Baan *et al.* measure an integrated flux density of 1.01×10^4 mJy km s⁻¹, while we measure 6.11×10^3 mJy km s⁻¹. The host of this OHM is classified a Seyfert 2 by Kim, Veilleux, & Sanders (1998). Solomon *et al.* (1997) measure a CO(1–0) line width of 270 km s⁻¹, estimate a H₂ mass of $4.4 \times 10^{10} M_{\odot}$, and derive a blackbody radius of 284 pc.

14553+1245: This OHM has a well-defined second peak in the ACF which agrees with the 1667 MHz prediction for the 1665 MHz line, but there is no clear spectral feature. We use the noise to set an upper bound on the 1665 MHz line and a lower bound on the hyperfine ratio: using 1σ and the width of 1667 line, $R_H \geq 14.5$. The main OH line sits atop broad low-level emission which is included in the measure of the total OH emission, while measurements of the 1667 MHz line use only the most obvious feature.

14586+1432: The spectrum of this OHM is extremely broad and complicated. The FWHM listed in Table 6 is measured from the central (double) peak, but the FWHM of the entire complex is 950 km s⁻¹ in the rest frame. The total line complex spans 1160 km s⁻¹ (rest frame) at 10% of peak flux density. The ACF is very smooth and shows no second peak due to the blending of emission lines. The weights spectrum indicates some narrow RFI on the edge of the OH profile which does not significantly affect the spectrum. One interpretation of this complicated spectrum is straightforward: there are two nuclei in this object, both of which are masing. We label nucleus A the higher velocity nucleus, and nucleus B the lower velocity nucleus. Going from right to left in the OH spectrum, we see the peaks corresponding to 1665A, 1667A, 1665B (on the shoulder of 1667A), and 1667B. The predicted locations of the 1665 MHz lines from the positions of the 1667 MHz lines agrees nicely with the actual emission peaks, and there is an uncanny correspondence of features between 1667A and 1665A. The optical redshift favors nucleus A, and we use 1667A to measure v_{1667} in Table 6. The two nuclei have a velocity difference of 516 km s⁻¹ in the rest frame. We use the entire complex to compute W_{1667} , which is an upper limit because it includes 1665 MHz emission.

17161+2006: This OHM shows a strong main line and only weak evidence for a 1665 MHz line. There is a weak second peak in ACF which corresponds with the predicted location of the 1665 MHz line from the center of the 1667 MHz line. The ACF was computed after masking the deep RFI trough at 31850 km s⁻¹. The weights spectrum is clean across the OH lines. The identification of the 1665 MHz line is tentative, and resembles other baseline features, making the hyperfine ratio uncertain.

4.3.2. Notes on OH Absorbers

12107+3157: This is an OH absorber, but unlike IRAS 19154+2704 (see Paper I), there is no obvious 1665 MHz line, and no second peak in the ACF. The absorption feature is broad (420 km s⁻¹ in the rest frame), but the signal to noise of this spectrum is low, so potentially interesting structure in the line will have to be confirmed by further observations. The NVSS flux is quite high for a ULIRG at $z = 0.2065$ (32 mJy), indicating that there is a radio loud nucleus in this object.

4.4. Survey Completeness

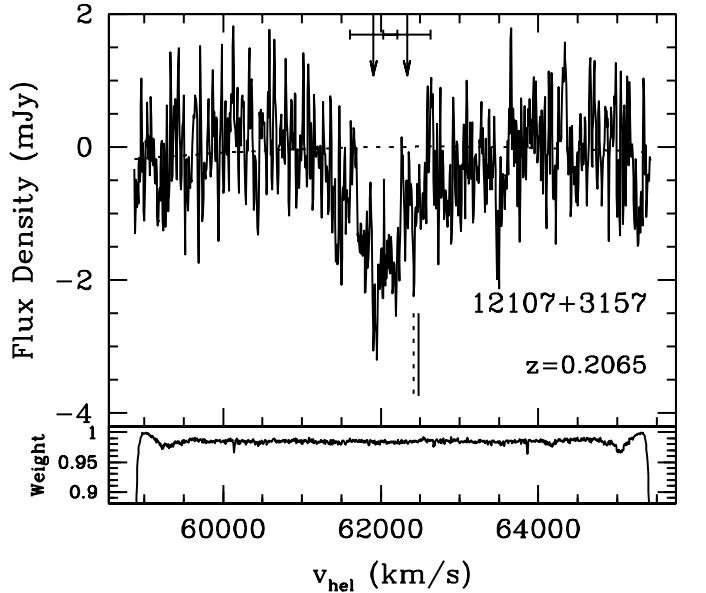


FIG. 2.— An OH Absorber Discovered in a ULIRG. This spectrum is presented in exactly the same manner as the OH megamaser detections (see Figure 1). The properties of this OH absorber is listed at the end of Tables 5 and 6.

The Arecibo OH megamaser survey is flux-limited and thus will not identify OHMs which fall below the detection threshold. How many OHMs is the survey missing? In order to predict the OH luminosity of OHM candidates in the survey, we employed the relation obtained by Kandalian (1996) from the then known OHM sample: $\log L_{OH}^{pred} = (1.38 \pm 0.14) \log L_{FIR} - (14.02 \pm 1.66)$. Rather than predicting L_{OH} of OHMs, the predicted OH luminosity seems to indicate a rough division between OHMs and nondetections, as shown in Figure 3 (since $\log L_{OH}^{pred} \propto \log L_{FIR}$, this figure is identical to Figure 6 — only the scale on the abscissa has changed). There is little overlap between the OHMs and the nondetections, indicating a well-defined line detection threshold, and there are likely to be OHMs remaining in the nondetections with $L_{OH} < 10^2 L_{\odot}$. Taking into account the OHM fraction as a function of L_{FIR} (see §5.3), the OH-FIR relation determined in §5.4, and the scatter in the relation, we estimate that there are roughly a dozen undetected OHMs lurking in the nondetections, nearly all of which have $L_{OH} < 10^2 L_{\odot}$.

5. THE HOSTS OF OH MEGAMASERS

The complete Arecibo OH megamaser survey has well-defined selection criteria and an adequate sample size for an investigation of the relationships between the flux-limited sample of OHMs and the merging systems which produce them. We investigate the OH megamaser fraction in (U)LIRGs as a function of their properties, the nature of the star formation in OHM hosts, and the relationships between the properties of OHMs and their hosts.

5.1. The Received View

All known OHMs have been observed in luminous infrared galaxies (LIRGs), strongly favoring the most FIR-luminous, the ultraluminous infrared galaxies (ULIRGs; Baan 1991). Photometric surveys have shown the ULIRGs

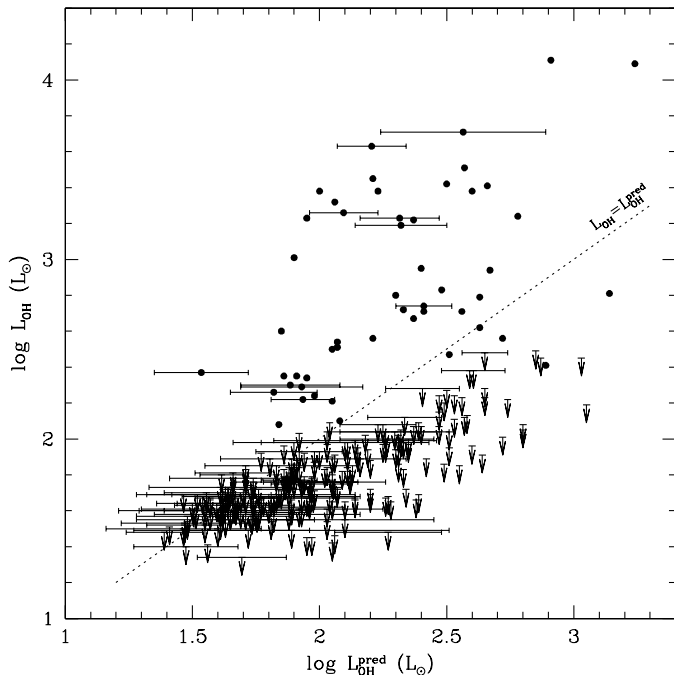


FIG. 3.— Survey completeness: OH luminosity measurements versus predictions for all unambiguous survey targets. OH megamasers are plotted as filled circles and nondetections are plotted as inverted triangles to indicate upper limits on OH line luminosity. Horizontal error bars indicate objects with upper limits on $100\mu\text{m}$ detection; the bars span the available range of L_{FIR} set by the upper detection limit on $f_{100\mu\text{m}}$ and negligible $100\mu\text{m}$ flux. The heavy dashed line indicates the locus $L_{OH} = L_{OH}^{pred}$.

to be nearly exclusively the product of galaxy mergers (Clements *et al.* 1996). VLBI measurements have shown that OHMs are ensembles of many masing regions which originate in the nuclear regions of (U)LIRGs on scales of a few hundred parsecs or less (Diamond *et al.* 1999). OHM activity requires: (1) high molecular density, (2) a pump to invert the hyperfine population of the OH ground state, and (3) a source of 18 cm continuum emission to stimulate maser emission (Burdyuzha & Komberg 1990). The environments produced in merging galaxies can supply all of these requirements: the merger interaction concentrates molecular gas in the merger nuclei, creates strong FIR dust emission from reprocessed starburst light and AGN activity, and produces radio continuum emission from AGN and starbursts. The FIR radiation field can invert the OH population via the pumping lines at 35 and 53 μm ((Skinner *et al.* 1997)). Masing can then be stimulated by 18 cm continuum emission from starbursts or AGN, or even by spontaneous emission from the masing cloud itself (Henkel, Güsten, & Baan 1987).

Based on optical morphology and surface brightness profiles, the FIR luminosity of LIRGs seems to be correlated with the stage in a merger sequence such that late-stage mergers are the most FIR-luminous (Sanders, Surace, & Ishida 1999). The OHM fraction in LIRGs is a strong function of L_{FIR} (Baan 1991), which indicates that the later stages of merging may be preferred for OHM formation. This makes some physical sense, based on the high molecular gas density required to produce OHMs ($n_{H_2} = 10^{4-7} \text{ cm}^{-3}$; Baan 1991). Early in the merger sequence, infall and concentration of molecular gas in the nuclear regions is

just beginning, whereas late in the merger sequence, clouds are disrupted by ionizing radiation, a superwind phase, or a QSO eruption. If OHMs mark a specific phase in major mergers, then they provide useful tracers of the galaxy merger rate as a function of redshift, particularly since they may be observed at cosmological distances with current instrumentation (Baan 1989; Burdyuzha & Komberg 1990; Briggs 1998)

5.2. The Known OH Megamasers

The library of OHMs is incomplete and drawn from many disparate surveys, and a comprehensive study strictly from the literature is difficult. We present here a compilation of the known OHMs which is useful for discussing the received view about OHM environments and mechanisms, and which for the first time attempts to gather all of the available information into a single place and format. Baan, Salzer, & LeWinter (1998) present the largest compilation of OHMs available in the literature (50 objects). This includes 3 OHMs which do not appear anywhere else in the literature. To this list of 50 OHMs, we add 4 OHMs found in the literature. Of these 54 objects, 25 OHMs do not have published spectra, and 5 are highly suspect detections. Six of the OHMs listed are not technically OHMs ($L_{OH} = 10^1-10^4 L_{\odot}$) or OH “gigamasers” ($L_{OH} > 10^4 L_{\odot}$); they are OH “kilomasers.” Tables 7 and 8 summarize the optical redshifts and FIR properties and the OH and 1.4 GHz properties of the known OHMs (in the loose sense).

We make every effort to present uniform OHM data, which is made difficult by sparse and sometimes conflicting reporting of data. When measured properties conflict, we preferentially use the observations presented in detection papers. The peak flux density of the 1667 MHz OH line is generally not quoted in the literature. Data on the hyperfine ratio, the OH velocity, and the OH line width are most often lacking. In order to place the data into a uniform cosmology, we take observer units of integrated line flux, usually $\text{erg s}^{-1} \text{ cm}^{-2}$, and convert to a cosmology-dependent line luminosity.

Tables 7 and 8 list respectively the optical/FIR and radio properties of the 54 known OH megamasers and kilomasers (hereafter jointly referred to as OHMs). Table 7 lists the optical redshifts and FIR properties of the OHMs in a format identical to Table 1. Table 8 lists the OH luminosity, 1.4 GHz flux density, and nuclear classification of the known OHMs in the following format: Column (1) lists the *IRAS* FSC name, as in Table 7. Column (2) lists the heliocentric optical redshift, as in Table 7. Column (3) lists the $\log L_{FIR}$, as in Table 7. Column (4) lists the predicted isotropic OH line luminosity, $\log L_{OH}^{pred}$, based on the Malmquist bias-corrected $L_{OH}-L_{FIR}$ relation determined by Kandalian (1996) from 49 OHMs: $\log L_{OH} = (1.38 \pm 0.14) \log L_{FIR} - (14.02 \pm 1.66)$ (see §5.4). Column (5) lists the logarithm of the measured isotropic OH line luminosity, which includes the integrated flux density of both the 1667.359 and the 1665.4018 MHz lines. Note that L_{OH}^{pred} is generally less than the actual L_{OH} detected (42 out of the 51 objects with available OH measurements). Column (6) lists the peak flux density of the 1667 MHz OH line in mJy. Column (7) lists references for the listed OH line properties. Column (8) lists the 1.4

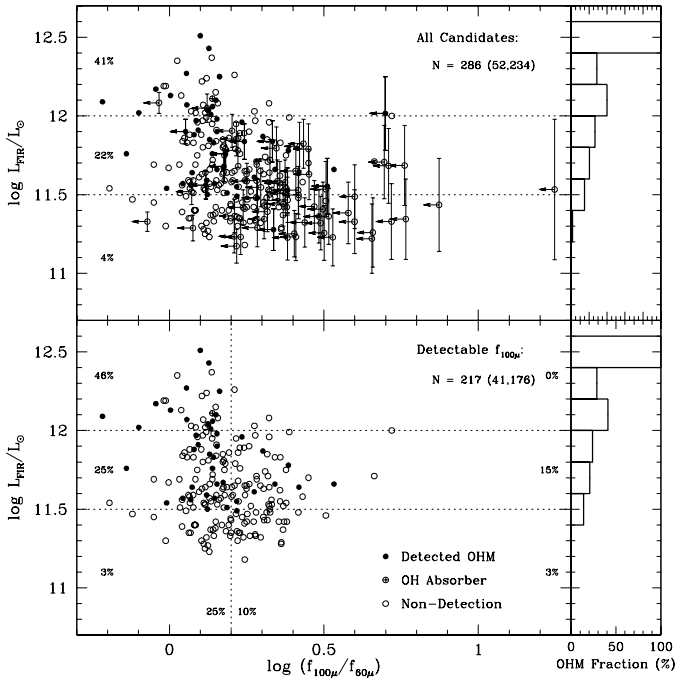


FIG. 4.— The Arecibo OH megamaser survey FIR color-luminosity plots. The two left panels show L_{FIR} versus FIR color for candidates observed to date, and the two right panels show the OHM fraction as a function of L_{FIR} . Filled circles mark OHMs, empty circles mark non-detections, and the crossed circle marks the OH absorber. Points with error bars are non-detections at $100\ \mu\text{m}$. Vertical error bars indicate the possible range of L_{FIR} , constrained by $f_{60\mu\text{m}}$ and an upper limit on $f_{100\mu\text{m}}$. Horizontal arrows indicate upper limits on FIR color. Inset percentages indicate the OHM fraction for each sector delineated by the dashed lines. The upper panels plot all 286 candidates observed. The lower panels plot the 217 objects with detected $f_{100\mu\text{m}}$. The inset numbers follow the key: N = Observed (OHMs, Non-Detections).

GHz continuum fluxes, from the NRAO VLA Sky Survey (NVSS; Condon et al. 1998). If no continuum source lies within $30''$ of the *IRAS* coordinates, an upper limit of 5.0 mJy is listed. Note that sources south of -40° declination are not included in the NVSS. Column (9) lists the optical spectroscopic classification, if available: (S1) Seyfert 1, (S1.5) Seyfert 1.5, (S2) Seyfert 2, (A) active nucleus, (C) composite active and starburst nucleus, (H) HII region (starburst), and (L) low-ionization emission region (LINER). References for the classifications are shown in parentheses and included at the foot of the table. Column (10) lists source notes, which are given at the foot of the table.

5.3. The FIR Luminosities and Colors of OH Megamaser Hosts

The Arecibo OHM survey detected 1 OHM in every 5.5 candidates, but the OHM fraction is not constant across all LIRGs as shown in Figure 4. The OHM fraction is a strong function of L_{FIR} , increasing to at least one in three for ULIRGs. A similar trend was quantified by Baan (1991). Clearly, some property of the most luminous LIRGs promotes OHM production. Note also that nearly half of the LIRGs in the upper left quadrant of the lower plot in Figure 4 host OHMs, indicating a color dependence on OHM production as well. This color dependence was also noted by Unger *et al.* (1986), Staveley-Smith *et al.* (1992), Baan,

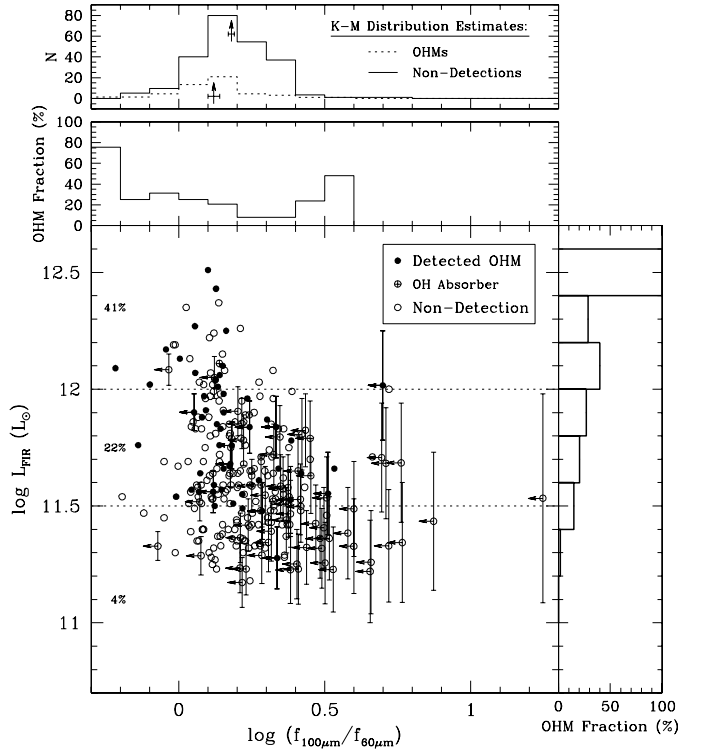


FIG. 5.— The OH megamaser fraction by FIR luminosity and color. The main panel shows L_{FIR} versus FIR color for unambiguous OHM candidates, the right panel shows the OHM fraction as a function of L_{FIR} , the topmost panel shows the color distribution of OHMs and nondetections estimated by a survival analysis, and the middle panel shows the estimated OHM fraction as a function of FIR color. Points with error bars are non-detections at $100\ \mu\text{m}$. Vertical error bars indicate the possible range of L_{FIR} , constrained by $f_{60\mu\text{m}}$ and an upper limit on $f_{100\mu\text{m}}$. Horizontal arrows indicate upper limits on FIR color. Inset percentages indicate the OHM fraction for each sector delineated by the dashed lines. The arrows in the top panel indicate the mean and standard deviation survival analysis estimates for the OHM and nondetection populations.

Haschick, & Henkel (1992), and others.

There are indications in Figure 4 that LIRGs with “warmer” FIR colors (smaller $f_{100\mu\text{m}}/f_{60\mu\text{m}}$) are more likely to host OHMs. The top panel of Figure 4, which plots all unambiguous objects in the survey, shows that a quarter of the objects are undetected by *IRAS* in the $100\ \mu\text{m}$ band. A proper analysis of the heavily censored FIR color of OHM hosts requires survival analysis techniques which can properly account for upper limits on measured quantities. These techniques are available in the IRAF ASURV package Rev 1.2 (LaValley, Isobe, & Feigelson 1992), which implements the methods presented in Feigelson & Nelson (1985). The tests employed by ASURV find a difference between the colors of OHM hosts and nondetections at the 0.5–1.4% significance level, and the Kaplan-Meier estimates of the mean colors $\log(f_{100\mu\text{m}}/f_{60\mu\text{m}})$ are 0.12 ± 0.02 for the OHM hosts and 0.18 ± 0.01 for the non-detections. Hence, despite the obfuscation of the upper limits on colors, the apparent preference for warm LIRGs to produce OHMs is confirmed with high confidence.

Figure 5 shows the FIR color-luminosity plot of all unambiguous survey objects with the OHM fraction as a function of both luminosity and color. The fraction versus color is derived from the Kaplan-Meier estimates of the differential distribution of the OHMs and the nonde-

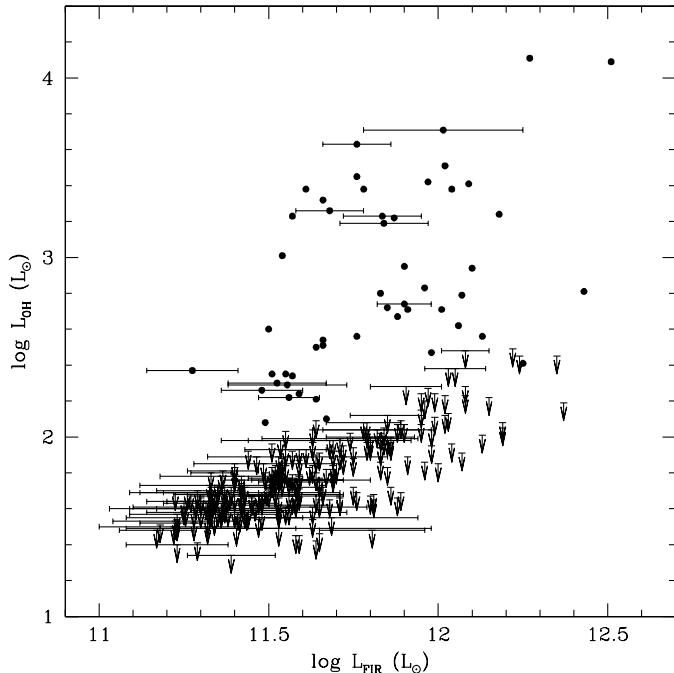


FIG. 6.— The Arecibo OH Megamaser Survey: L_{OH} versus L_{FIR} for all unambiguous survey targets. OH megamasers are plotted as filled circles and nondetections are plotted arrows to indicate upper limits on OH line luminosity. Horizontal error bars indicate objects with upper limits on $100\mu\text{m}$ detection; the bars span the available range of L_{FIR} set by the upper detection limit on $f_{100\mu\text{m}}$ and negligible $100\mu\text{m}$ flux.

tections. These distributions are plotted in the top panel of Figure 5. Note that the OHM fraction, while large at the highest and lowest color values, is derived from very few objects. The reliable and noteworthy information contained in this analysis is the strong rise in the fraction of OHMs with warmer color from $\log(f_{100\mu\text{m}}/f_{60\mu\text{m}})$ values of ~ 0.4 to ~ 0 . This is also apparent in the differing shapes of the estimated distributions of OHMs versus nondetections. We confirm that LIRGs with warmer FIR colors — and hence higher dust temperatures — are more likely to produce OHMs. ULIRGs generally have higher dust temperatures than the less luminous LIRGs, so there may be some entanglement of the roles of L_{FIR} and FIR color in producing OHMs. It is unclear if the two effects can be disentangled. Higher dust temperatures and higher luminosities will both increase the number of photons available to pump OH molecules, so they may both be related to L_{OH} .

5.4. The FIR-OH Relationship

Suppose that an OH maser is radiatively pumped by the FIR radiation field. In a simple scenario of low gain unsaturated masing, the maser output is proportional to the pumping rate and to the stimulated emission rate (Baun 1989). If the pump is the FIR radiation field, and the source of stimulated emission is the radio continuum field, which is itself proportional to the FIR radiation field in star-forming regions (Yun, Reddy, & Condon 2001), then the observed maser output can be related to a single parameter: $L_{OH} \propto L_{FIR} L_{1.6\text{GHz}} \propto L_{FIR}^2$. For the case of low gain saturated masing, the stimulant cannot be fully accommodated by the inverted gas, and drops out of the

relation: $L_{OH} \propto L_{FIR}$. If we suppose that an OH megamaser represents an ensemble of many individual masing regions with different saturation states, then it is reasonable to expect that $L_{OH} \propto L_{FIR}^\gamma$, where $1 < \gamma < 2$. The measurement of γ has traditionally been frustrated by small samples, survey biases, and theoretical predisposition. However, Kandalian (1996) demonstrated that a simple regression of the available OHM data indicates $\gamma = 1.66$, and when one properly accounts for Malmquist bias (i.e. the correlation of L_{OH} and L_{FIR} with distance in flux-limited surveys), the relationship becomes more linear: $\gamma = 1.38 \pm 0.14$. VLBI observations of a few individual OHMs by Diamond *et al.* (1999) support the statistical results. They find that OHM emission is likely to be segregated into two emission regimes: unsaturated extended emission and high gain saturated compact (< 1 pc) masing regions. As seems reasonable, OHMs appear to represent an aggregate of a broad range of masing conditions.

Although the assumption of low gain masing in all OHMs and the use of γ as a saturation index ($\gamma = (2)1$ for (un)saturated masing) is not supported by observations, we examine the empirical relationships between L_{OH} , L_{FIR} , $L_{60\mu\text{m}}$, and $L_{1.4\text{GHz}}$ to identify and quantify trends in the OHM sample. Recall the basic relationship for masing under scrutiny:

$$L_{OH} \propto L_{FIR} L_{1.6\text{GHz}}^{\gamma-1}. \quad (2)$$

This assumes radiative pumping. A good proxy for $L_{1.6\text{GHz}}$ is $L_{1.4\text{GHz}}$, a proxy for L_{FIR} is $L_{60\mu\text{m}}$, and the radio continuum-FIR relationship for star forming galaxies provides a nearly linear relationship between $L_{1.4\text{GHz}}$ and $L_{60\mu\text{m}}$ (Yun, Reddy, & Condon 2001; see §5.5). Hence, we make several different determinations of γ from fits to L_{OH} versus L_{FIR} , L_{OH} versus $L_{60\mu\text{m}}$, and $L_{OH}/L_{60\mu\text{m}}$ versus $L_{1.4\text{GHz}}$. These fits require progressively fewer assumptions about the validity of the relationships between luminosities. We determine the OH-FIR relation of OHMs first from the Arecibo survey sample, then from the sample of all available OHMs.

5.4.1. Arecibo Survey OHMs

This sample includes all 52 OHMs detected in the Arecibo OHM survey, including 3 redetections (*IRAS* 10378+1108, 12018+1941, and 14070+0525). The Arecibo survey is flux-limited, which indicates that there may be undetected OHMs still lurking in the sample. Figure 6 shows the OH-FIR relation for all unambiguous survey targets, plotting OH nondetections as upper limits on L_{OH} . There is little overlap between the body of OHMs and nondetections in this plot, indicating that the detection threshold is well-defined. Note that a flux limit in a spectral line survey does not correspond cleanly to a luminosity limit at a fixed distance when the variation of line profiles is large.

Figure 7 plots the three permutations of the OH-FIR relationship for the Arecibo OHM sample with fits indicated by dotted lines and labeled by their slopes. Also plotted is the radio continuum-FIR relation for the sample with a dotted line indicating the relationship derived by Yun, Reddy, & Condon (2001). *This line is not a fit.* Upper limits on the radio continuum luminosity derived from the NVSS are indicated by arrows. The data for these plots can be found in Tables 5 and 6 and the equivalent tables in Paper I and Paper II.

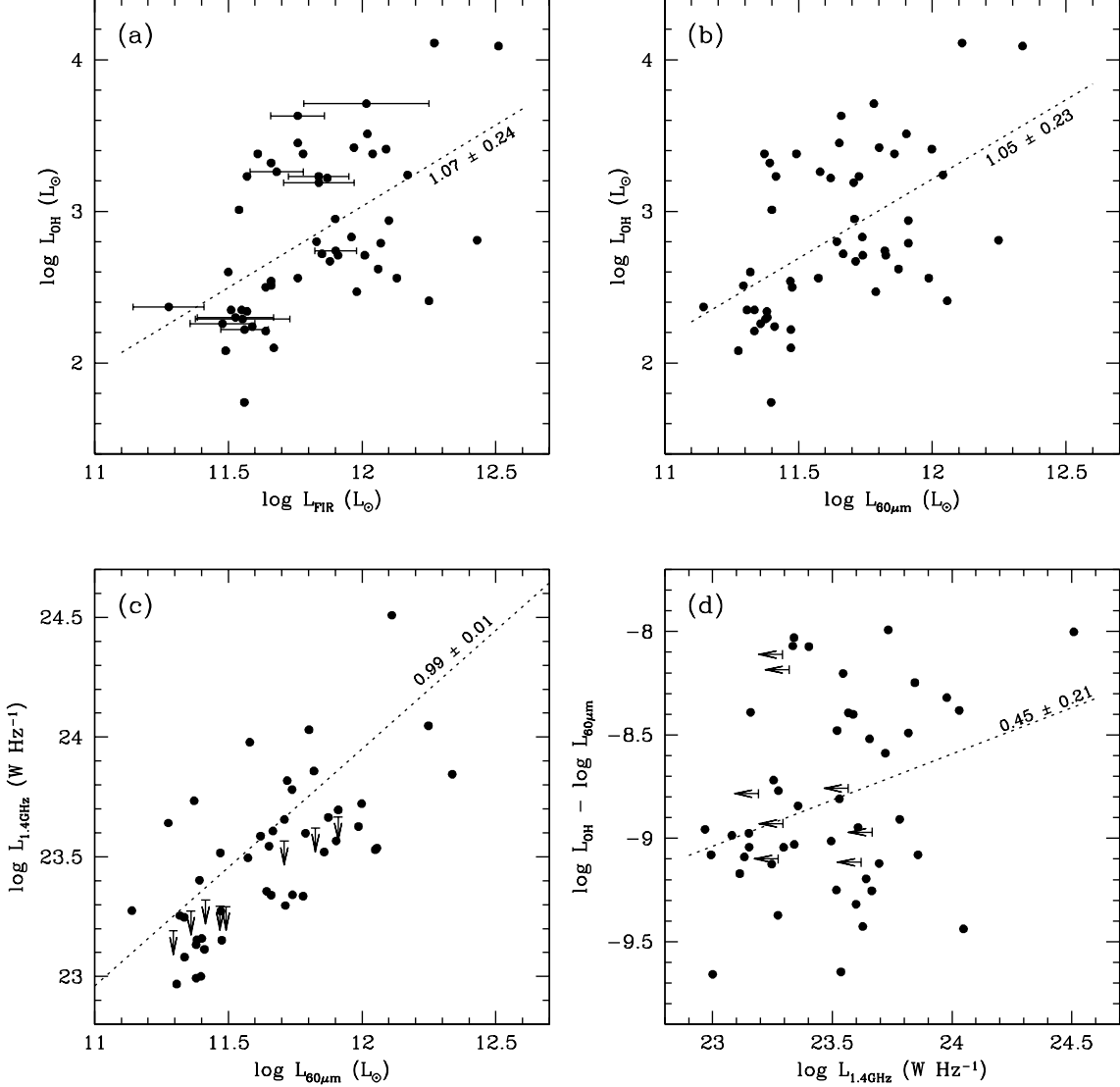


FIG. 7.— OH-FIR-Radio relations of Arecibo survey OH megamasers. Upper limits are indicated by arrows, and the available ranges for L_{FIR} are indicated by error bars. Dotted lines are fits to the data labeled by their slopes except for the $L_{1.4GHz}$ versus $L_{60\mu m}$ plot which is *not* at fit to the data but instead shows the radio-FIR relation obtained from a large sample of galaxies spanning many decades in luminosity (Yun, Reddy & Condon 2001). Shown are (a) the OH-FIR relation, (b) the OH-60 μm relation, (c) the radio-60 μm relation, and (d) the unbiased OH-60 μm -radio relation.

OH-FIR: L_{OH} and L_{FIR} are not well-correlated ($R = 0.53$), despite their mutual correlation with distance (see Figure 7). Also, L_{OH} is not as correlated with distance as is L_{FIR} : $R(L_{OH}, D_L) = 0.57$; $R(L_{FIR}, D_L) = 0.79$. A simple fit finds the relation $\log L_{OH} = (1.07 \pm 0.24) \log L_{FIR} - (9.81 \pm 2.85)$. However, since both L_{OH} and L_{FIR} are correlated with luminosity distance D_L , the partial correlation coefficient⁵ of L_{OH} with L_{FIR} at fixed D_L further reduces the OH-FIR correlation to non-significance: $R = 0.16$. The regression corrected for Malmquist bias obtains $\gamma = 0.32$. Note that the correlation of L_{OH} with L_{FIR} at fixed D_L is not equivalent to the correlation between OH and FIR fluxes because each object lies at a different distance.

OH-60 μm : Analysis of the relationship between L_{OH}

⁵ The partial correlation coefficient between x and y at fixed z is $R_{x,y,z} = \frac{R_{xy} - R_{xz}R_{yz}}{\sqrt{(1-R_{xz}^2)(1-R_{yz}^2)}}$ where R_{ij} is the standard correlation coefficient.

and $L_{60\mu m}$ produces nearly identical results to the L_{OH} - L_{FIR} analysis, despite the notion that the 60 μm luminosity is a more relevant diagnostic of the radiative IR pumping lines of the OH molecule at 35 and 53 μm . Again, L_{OH} and $L_{60\mu m}$ are not well-correlated ($R = 0.54$), despite the mutual correlation with distance, and L_{OH} is not as correlated with distance as is L_{FIR} : $R(L_{OH}, D_L) = 0.57$; $R(L_{FIR}, D_L) = 0.80$. The uncorrected fit produces the relation $\log L_{OH} = (1.05 \pm 0.23) \log L_{60\mu m} - (9.35 \pm 2.69)$. The corrected correlation is not significant ($R = 0.16$) and the corrected slope is $\gamma = 0.32$.

OH-60 μm -Radio: Since the OHMs in the sample might not exactly follow the radio-FIR relationship, assuming $L_{FIR} \propto L_{1.4GHz}$ may introduce extra scatter into the OH-FIR relation. Instead — still assuming that the maser is radiatively pumped — we investigate the dependence on the radio emission, which is directly related to the saturation state of the maser. Rearranging Equation 2, and using the 1.4 GHz radio continuum luminosity as a

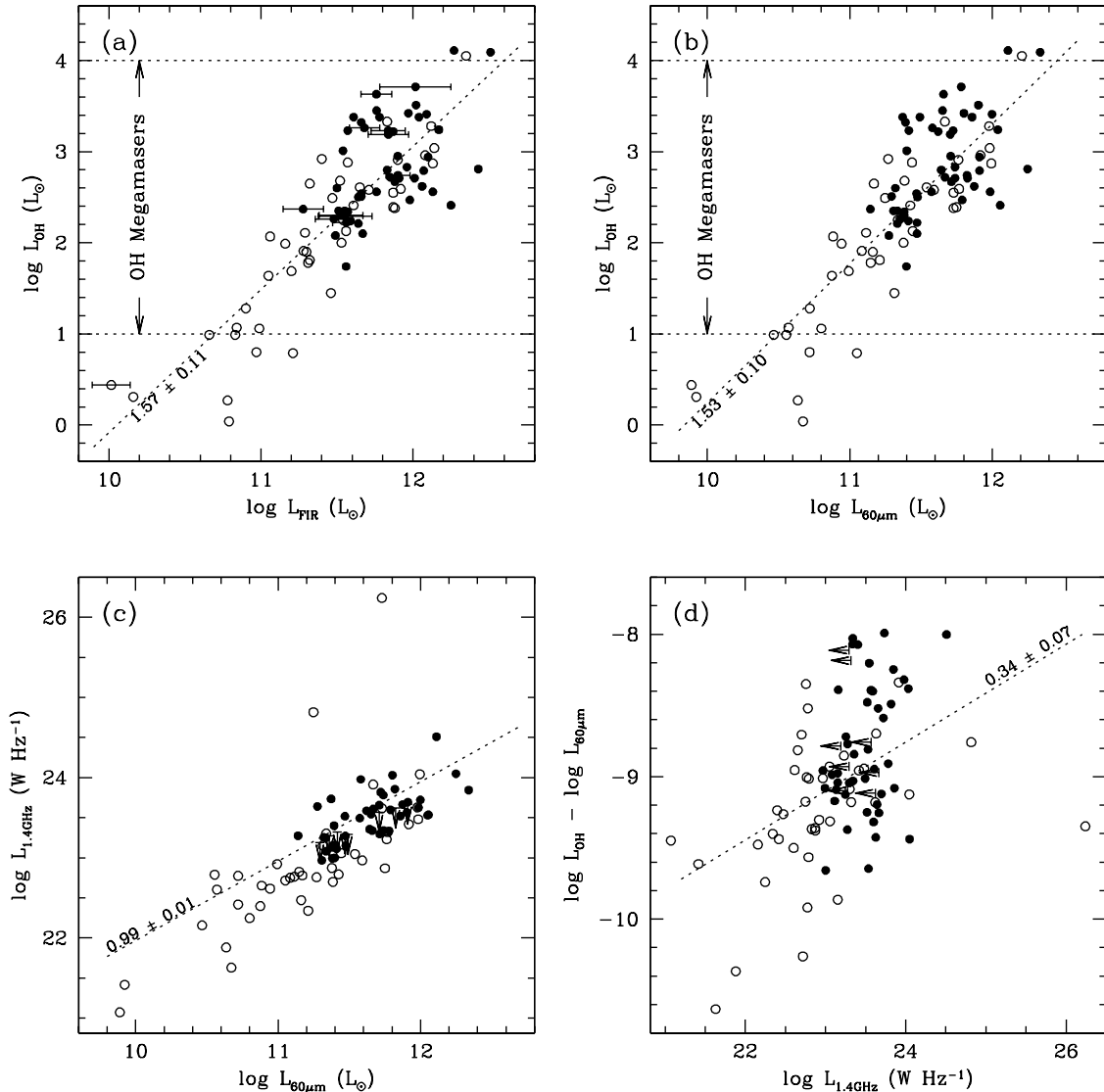


FIG. 8.— OH-FIR-Radio relations of all OH megamasers. Filled circles indicate Arecibo survey detections (including 3 previously discovered OHMs) and open circles mark previously known OHMs. Upper limits are indicated by arrows, and the available ranges for L_{FIR} are indicated by error bars. Dotted lines are fits to the data labeled by their slopes except for the $L_{1.4GHz}$ versus $L_{60\mu m}$ plot which is *not* a fit to the data but instead shows the radio-FIR relation obtained from a large sample of galaxies spanning many decades in luminosity (Yun, Reddy & Condon 2001). Shown are (a) the OH-FIR relation, (b) the OH-60 μm relation, (c) the radio-60 μm relation, and (d) the unbiased OH-60 μm -radio relation.

good proxy for the stimulating radiation, we obtain a relationship which is not subject to Malmquist bias and which incorporates more information about the masing process:

$$\log L_{OH} - \log L_{60\mu m} = (\gamma - 1) \log L_{1.4GHz} + \beta. \quad (3)$$

All units are absorbed into the β term. Requiring radio continuum detections in the NVSS reduces the sample to 41 new OHMs and 3 redetections (44 total). Upper limits on radio luminosity are shown as arrows in Figure 7. Fits do not incorporate OHMs with upper limits on radio luminosity. The correlation between $\log L_{OH}/L_{FIR}$ and $\log L_{1.4GHz}$ is poor ($R = 0.31$) and the measured slope yields $\gamma = 1.45 \pm 0.21$.

5.4.2. Arecibo Survey + Known OHMs

Redetections of previously known OHMs are given the OH values measured in the survey. We do not wish to take credit away from those who discovered these objects, but

do favor including the higher signal to noise measurements of the Arecibo OHM survey. Using the values measured in the survey also enhances the uniformity of the sample for these analyses. There are 43 previously known OHMs, 49 new OHMs, and 3 redetections (95 data points) in this expanded sample. Figure 8 reproduces Figure 7 for the expanded sample with the two OHM subsets as labeled. The data for the previously identified OHMs can be found in Tables 7 and 8.

OH-FIR: L_{OH} and L_{FIR} are well-correlated ($R = 0.84$), and are correlated with distance: $R(L_{OH}, D_L) = 0.71$; $R(L_{FIR}, D_L) = 0.74$. A fit obtains the relation $\log L_{OH} = (1.57 \pm 0.11) \log L_{FIR} - (15.76 \pm 1.22)$. Unlike the Arecibo OHM sample alone, the combined sample retains a significant OH-FIR correlation after Malmquist bias correction: $R = 0.66$. The corrected slope in the relation is shallower than the simple fit slope, at $\gamma = 1.24$.

OH-60 μ m: Analysis of the relationship between L_{OH} and $L_{60\mu m}$ again produces nearly identical results to the L_{OH} - L_{FIR} analysis. L_{OH} and $L_{60\mu m}$ are correlated with each other and with distance: $R = 0.84$; $R(L_{OH}, D_L) = 0.71$; $R(L_{60\mu m}, D_L) = 0.72$. The uncorrected fit obtains the relation $\log L_{OH} = (1.53 \pm 0.10) \log L_{60\mu m} - (15.04 \pm 1.19)$, and the corrected fit retains correlation between L_{OH} and $L_{60\mu m}$ ($R = 0.66$) and has a slope of $\gamma = 1.21$.

OH-60 μ m-Radio: Requiring radio continuum detections in the NVSS reduces the sample to 41 previously known OHMs, 41 new OHMs, and 3 redetections (85 total). Upper limits on the radio continuum luminosity are shown as arrows in Figure 8. Fits do not incorporate OHMs with upper limits on the radio luminosity. The correlation between $\log L_{OH}/L_{FIR}$ and $\log L_{1.4GHz}$ is again poor ($R = 0.46$) and the measured slope yields $\gamma = 1.34 \pm 0.07$.

5.4.3. Discussion

As indicated by the poor correlation between variables in the fits of Arecibo survey OHMs, the intrinsic scatter in the OH-FIR relation is similar to the span of the survey in L_{FIR} and L_{OH} . Because the survey work was strictly above $z = 0.1$, only the upper end of the LIRG population was sampled, which does not provide an adequate lever arm to extract a useful relationship from the intrinsic scatter in the OH-FIR relationship. Expanding the sample to all known OHMs provides the span in L_{FIR} and L_{OH} required to resolve the relationship.

The relationship derived from the expanded sample reveals a similar slope for all three permutations of the OH-FIR relation. We adopt a final form for the Malmquist bias-corrected relation which applies to both L_{FIR} and $L_{60\mu m}$:

$$\log L_{OH} = (1.2 \pm 0.1) \log L_{FIR} - (11.7 \pm 1.2). \quad (4)$$

The slope of this relation is even shallower than the value determined from the previously known OHM sample by Kandalian (1996). The value of $\gamma = 1.2$ suggests that either most OHMs are nearly saturated or that global properties of mergers such as L_{FIR} are not completely relevant to the production of OHMs on small scales. The latter conclusion is supported by the large scatter in the OH-FIR relationship. The dependence of OHM fraction on L_{FIR} indicates that global properties are important in setting up the right conditions for megamasers, but global properties are unlikely to determine the properties of the OHMs produced. These notions are supported by the poor trends of optical, FIR, and radio nuclear properties with OH emission line properties discussed below and in Paper V. The extra scatter introduced to the OH-FIR relation by folding in the radio continuum data indicates that either OHMs are nearly saturated or that most of the radio continuum is emitted from regions which are not associated with masing (or both).

5.5. The FIR-Radio Continuum Relationship

A well-known relationship exists between the FIR and radio continuum luminosities of star forming galaxies which spans roughly 5 orders of magnitude. Yun, Reddy, & Condon (2001) derive the form of the relationship from the 2 Jy *IRAS* sample (Strauss *et al.* 1992):

$$\log L_{1.4GHz} = (0.99 \pm 0.01) \log L_{60\mu m} + (12.07 \pm 0.08) \quad (5)$$

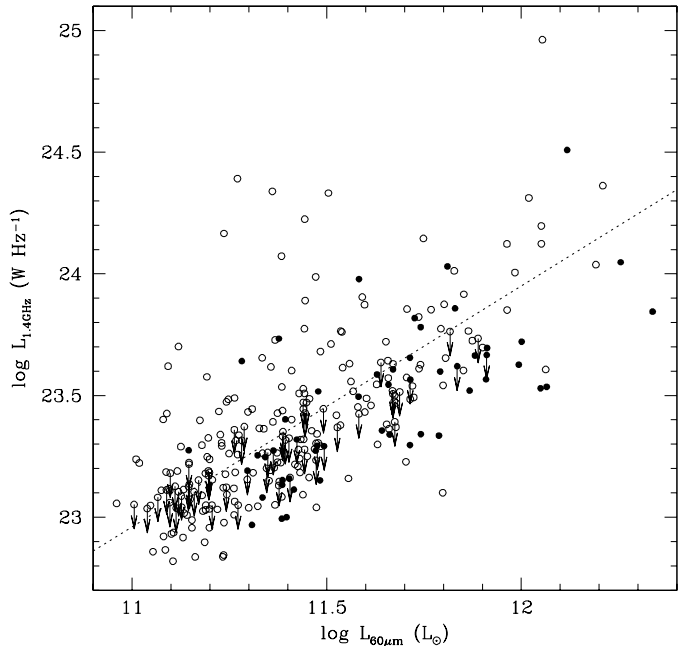


FIG. 9.— The radio-FIR correlation of the Arecibo survey. The dotted line is the radio-FIR correlation fit by Yun, Reddy, & Condon (2001) and is *not a fit* to the data. Filled circles are OH megamasers and open circles are OH nondetections. Upper limits on $L_{1.4GHz}$ obtained from the NVSS are indicated by arrows.

where $L_{1.4GHz}$ is in units of $W Hz^{-1}$ and $L_{60\mu m}$ is in solar luminosities. Figure 9 presents the radio-60 μ m relationship for the Arecibo OHM survey, including OH nondetections. The line on the plot is *not a fit* to the data; it is Equation 5. Figure 9 shows that there are some radio “monsters” in the sample and that there appears to be a trend for OHMs to be radio under-luminous (or IR over-luminous) compared to the Arecibo survey LIRG sample population as a whole. This may be a hint at the underlying properties of the interacting galaxies which favor OHM production, but analysis is complicated by the upper limits on radio continuum luminosity.

To more easily study departures of star forming galaxies from the FIR-radio continuum relationship many groups examine the “ q ” parameter (Condon *et al.* 1991) which is a measure of the logarithmic FIR to radio flux density ratio:

$$q \equiv \log \left(\frac{2.58 f_{60\mu m} + f_{100\mu m}}{2.98 \times 10^{26} Jy} \right) - \log \left(\frac{f_{1.4GHz}}{W m^{-2} Hz^{-1}} \right). \quad (6)$$

We define a variation on the q parameter called q' which does not depend on the *IRAS* 100 μ m flux:

$$q' \equiv \log \left(\frac{f_{60\mu m}}{1.15 \times 10^{26} Jy} \right) - \log \left(\frac{f_{1.4GHz}}{W m^{-2} Hz^{-1}} \right). \quad (7)$$

This version of the q parameter is favored because many of the LIRGs in the Arecibo OHM survey are not detected by *IRAS* at 100 μ m. Also, we can insert the radio-FIR relation of Equation 5 into Equation 7 to obtain the average q' value versus $L_{60\mu m}$ and compare it to the sample of OHMs and nondetections:

$$\bar{q}' = 0.01 \log \left(\frac{L_{60\mu m}}{L_{\odot}} \right) + 2.00. \quad (8)$$

The Arecibo OHM survey data spans $L_{60\mu m} = 10^{11} - 10^{12.4} L_{\odot}$, over which \bar{q}' changes by 0.01, which is within

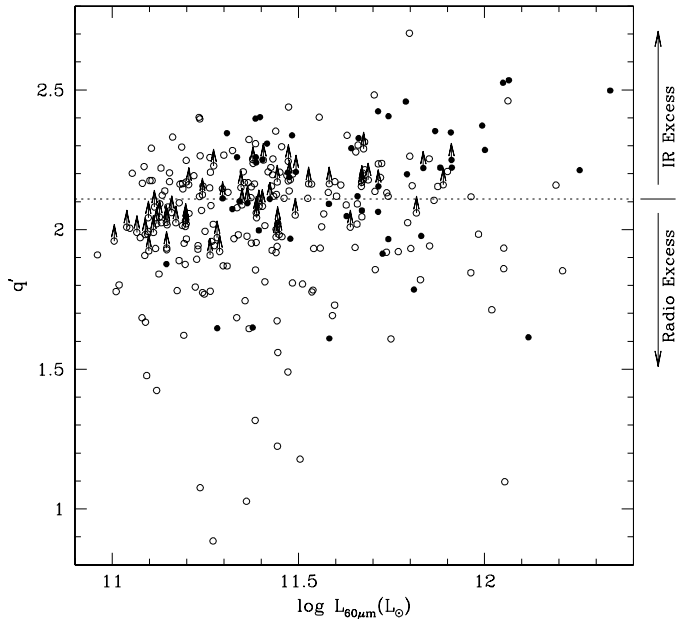


FIG. 10.— Radio/IR excess versus $L_{60\mu m}$. The q' statistic is a logarithmic measure of the $60\mu m$ to radio flux density ratio and is independent of distance. Upper limits on radio flux density correspond to lower limits on q' , as indicated by the arrows. Filled circles are OH megamasers and open circles are OH nondetections. The dotted horizontal line is $\bar{q}' = 2.11$ derived from the fit of a large sample of star forming galaxies by Yun, Reddy, & Condon (2001).

the uncertainty of the radio-FIR correlation. We set $\bar{q}' = 2.11$, the value at $L_{60\mu m} = 10^{11.7} L_{\odot}$. Figure 10 shows the distribution of q' values for the Arecibo survey sample, including sources which were not detected by the NVSS and thus have lower bounds for q' .

Cursory examination of Figure 10 indicates that OHMs may as a population have an IR excess compared to the OH nondetections. To include the upper limits on radio flux density, we perform a survival analysis. Using survival analysis techniques available in the IRAF ASURV package Rev 1.2 (LaValley, Isobe, & Feigelson 1992), which implements the methods presented in Feigelson & Nelson (1985), we obtain Kaplan-Meier estimates of the means and standard deviations of the q' values for the OHMs of 2.19 ± 0.03 and for the nondetections of 2.06 ± 0.02 . These appear to be statistically different populations among the LIRGs, with OHM hosts showing a IR excess compared to the nondetections. Rather than simply comparing the means of the populations, one can use all of the information contained in the complete samples and compare the Kaplan-Meier maximum likelihood estimator of the q' distribution of the two samples, as shown in Figure 11. Also, we use ASURV to compute non-parametric test statistics to determine the probability that the two populations were drawn from the same underlying sample, similar to the Kolmogorov-Smirnov test. The variety of possible tests stems from their vulnerability to different censoring distributions, and a safe approach is to compute a variety of test statistics and compare the results bearing in mind the nature of the censoring distribution in the data. The available test statistics are Gehan’s generalized Wilcoxon test (both permutation and hypergeometric variance), the logrank test, the Peto & Peto generalized Wilcoxon test, and the Pet & Prentice generalized Wilcoxon test (Feigel-

son & Nelson 1985). In this case, the censoring distribution is the same for both populations, although it may not be completely random. The two-population test statistics unanimously determine that the two populations have different q' distributions to high significance (0.01–0.13% probability that the two populations are the same).

This is a surprising result relating the star formation properties of LIRGs to the production of OHMs: OH megamaser hosts have a IR excess or a radio deficit compared to the OH nondetections and the LIRG population overall. This could either indicate that OHM hosts have buried AGN which make an extra contribution to the total FIR budget, or that OHM hosts are undergoing a very recent/violent burst of star formation in which the radio emission has not yet “caught up.” In either case, this result is quite surprising because ostensibly OH emission is proportional to both FIR and radio luminosity (the pump and the stimulant, respectively), but it appears that OHMs prefer hosts with an extra-strong pump. The next logical question to ask is: Are OHM hosts IR overluminous or radio underluminous?

The same two-population survival analysis performed on the radio luminosity of the OHMs and nondetections reveals a difference between the populations, but at a much less significant level. The various test statistics converge on differing populations at the 2.5% significance level, and the Kaplan-Meier estimator of the mean value for $\log L_{1.4GHz}$ ($W Hz^{-1}$) is 23.45 ± 0.05 for OHM hosts and 23.35 ± 0.02 for nondetections (the difference between these is nonzero by only 2σ). Although there are no censored $60 \mu m$ data points in the survey sample, we perform the identical survival analysis on the $60 \mu m$ luminosity to compare to the results for q' and the radio luminosity. The relevant test statistics find a highly significant ($< 0.01\%$) difference between the populations, and the Kaplan-Meier estimator of the mean value for $\log L_{60\mu m}$ (L_{\odot}) is 11.64 ± 0.04 for the OHM hosts and 11.41 ± 0.02 for the nondetections. These large differences in the FIR properties of OHM hosts from the LIRG population overall were also illustrated in Figure 4 and discussed in §5.3. This preference for high FIR luminosity hosts appears to dominate the effect seen in the q' analysis, and indicates that the OHM hosts are not so much radio deficient as they are IR abundant. In other words, objects which are IR-overluminous are more likely to produce OHMs independent of the radio emission properties. This is consistent with the nearly saturated masing state of OHMs determined from the OH-FIR relation in §5.4.

If LIRGs with an IR excess favor OHM production, does the excess also relate to the properties of the OH emission? Figure 12 shows the distribution of q' versus L_{OH} for the Arecibo OHM sample. There is no obvious correlation, again showing that the global properties of LIRGs can indicate the likelihood of OHM production, but the properties of the OHMs produced tend to rely on smaller scale physics.

5.6. The Manifold of OH Megamasers and Their Hosts

5.6.1. Basic Relationships

Few unambiguous relationships are evident among the properties of OHMs and their hosts. In general, the scatter in any given parameter is large compared to measurement

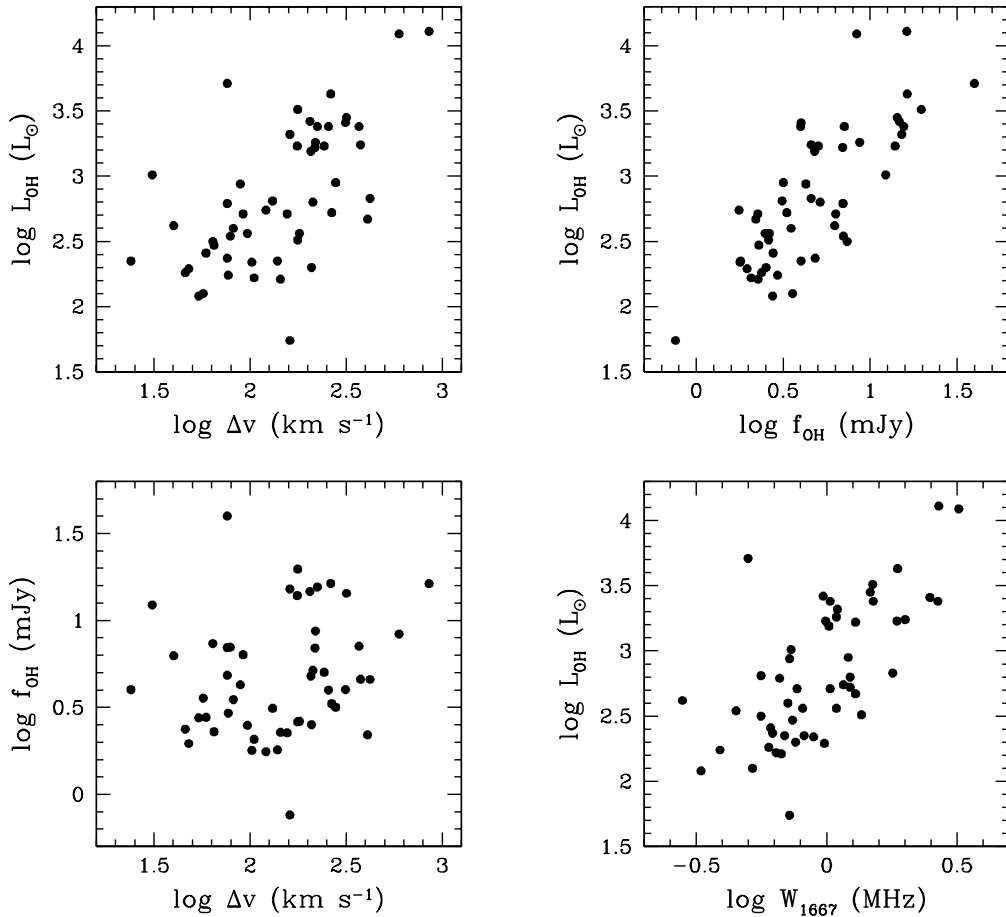


FIG. 13.— Relationships between OH line properties.

errors. Figure 13 plots various pairwise combinations of L_{OH} , Δv , W_{1667} , and f_{OH} . The most luminous OHMs tend to have the highest peak flux densities but are not necessarily broad. Line width and peak show very little correlation. One of the prominent outliers in these plots is *IRAS* 02524+2046, an exceptionally narrow but exceptionally strong OHM.

Two measures of OH pumping efficiency are plotted in Figure 14: the ratio of the peak OH flux density to the $60 \mu\text{m}$ flux density, and the ratio of the OH line luminosity to the $60 \mu\text{m}$ luminosity. Both measures show poor correlation with OH line width, unlike the result obtained by Staveley-Smith *et al.* (1992) which shows an anticorrelation (narrower OH lines have higher efficiency). Note that if $L_{\text{OH}}/L_{60\mu\text{m}}$ is constant with respect to Δv , then $f_{\text{OH}}/f_{60\mu\text{m}} \propto \Delta v^{-1}$ if the integrated flux density of the OH line obeys $F_{\text{OH}} \propto \Delta v f_{\text{OH}}$. Alternatively, if $f_{\text{OH}}/f_{60\mu\text{m}}$ is constant with respect to Δv , then $L_{\text{OH}}/L_{60\mu\text{m}} \propto \Delta v$. Figure 14 shows that the data favor the latter relationship, although we know from measuring OH profiles that the integrated OH line flux density can show a large variation for a given Δv due to the menagerie of emission profiles present in the OHM sample. The varied nature of the OH line profiles is likely to be the main source of the scatter in the relationship between $L_{\text{OH}}/L_{60\mu\text{m}}$ and Δv .

If the pumping efficiency measure $f_{\text{OH}}/f_{60\mu\text{m}}$ is constant with respect to Δv , what does this imply? It may

indicate that the line width is determined by the velocity structure in the gas produced by a merger while the frequency of maximum pumping efficiency is simply the velocity with the largest number of masers along the line of sight. In this scenario, the observed line profiles are a combination of the complicated gas dynamics found in the nuclei of merging systems and projection effects.

5.6.2. A Principal Component Analysis

A principal component analysis is made of (nearly) the same properties analyzed by Staveley-Smith *et al.* (1992): $\log f_{100\mu\text{m}}/f_{60\mu\text{m}}$, $\log L_{60\mu\text{m}}$, $\log \Delta v$ (the rest frame velocity width), $\log L_{\text{OH}}$, and $\log L_{1.4\text{GHz}}$. Minor differences reside in the measured radio luminosity (Staveley-Smith *et al.* define a radio luminosity spanning 0-10 GHz based on flux densities measured at 5 GHz), our use of $L_{60\mu\text{m}}$ instead of L_{FIR} , and the correction of the OH line width to the OHM rest frame. For 13 OHMs, Staveley-Smith *et al.* obtain a principal plane which accounts for 93% of the total variance in the sample and which reduces the RMS residuals in all parameters except L_{OH} to the estimated observational errors. Of the 52 OHMs in the Arecibo survey sample, 18 do not have measured *IRAS* $100 \mu\text{m}$ fluxes or were not detected in the NVSS, leaving 34 OHMs for this analysis. We used a principal component analysis code written by Murtagh, described by Murtagh & Heck (1987), and provided by the multivariate index of

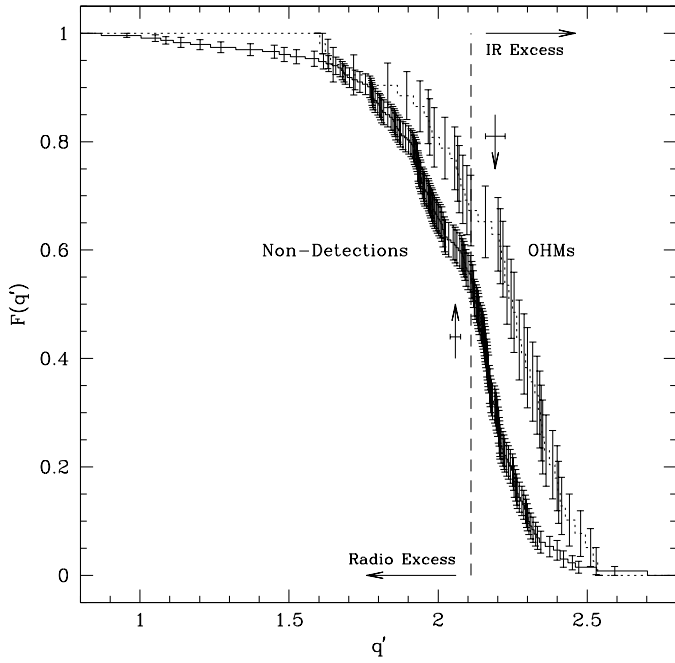


FIG. 11.— Estimated distributions of the radio/IR excess of OHMs and OH nondetections. The q' statistic is a logarithmic measure of the $60\mu\text{m}$ to radio flux density ratio and is independent of distance. $F(q')$ is the Kaplan-Meier survival analysis estimate of the distribution of q' , for which only lower limits exist for some objects in the survey. Shown are the distributions and estimated uncertainties for OHMs (dotted line) and the nondetections (solid line). The vertical dashed line indicates $\bar{q}' = 2.11$ derived from the fit of a large sample of star forming galaxies by Yun, Reddy, & Condon (2001). The vertical arrows indicate the Kaplan-Meier estimates of the mean and standard deviation of the two populations.

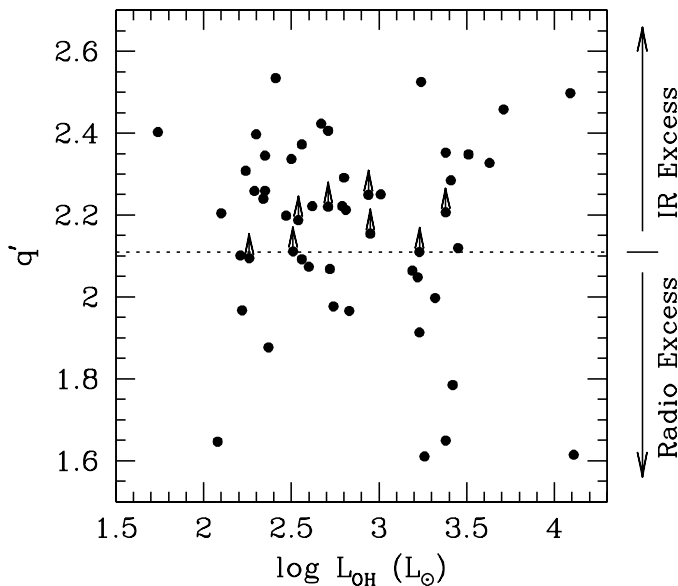


FIG. 12.— Radio/IR excess versus L_{OH} . The q' statistic is a logarithmic measure of the $60\mu\text{m}$ to radio flux density ratio and is independent of distance. Upper limits on radio flux density correspond to lower limits on q' , as indicated by the arrows. The dotted horizontal line is $\bar{q}' = 2.11$ derived from the fit of a large sample of star forming galaxies by Yun, Reddy, & Condon (2001).

analysis in the same manner as the Staveley-Smith *et al.* analysis for ease of comparison, including the correlation matrix, all of the eigenvectors and eigenvalues, all of the RMS residuals for progressively higher order fits, and the estimated observational errors in each parameter.

The correlation matrix indicates positive relationships between the OH, FIR, and radio luminosities as well as between the OH line width and the OH and radio luminosities. Recall that the luminosities are correlated in part due to Malmquist bias. FIR color exhibits only weak anti-correlations with the other parameters. Comparison of the RMS residuals to the observational errors indicates that the data set is not well described by a principal axis or principal plane. Only a 3-plane begins to bring the RMS residuals down to the level of the observation errors with the exception of L_{OH} . A similar extra variance in L_{OH} is seen by Staveley-Smith *et al.* (1992) which they interpret to indicate that OH masing relies on hidden variables such as beaming. The first few eigenvectors are not terribly illuminating either. The first principal component, which accounts for 56% of the variance, gets a uniform contribution from all variables except the color term. The second component draws mostly from the FIR color and the OH line width and accounts for 20% of the variance. The third component gets a nearly uniform contribution from all parameters but with the width and L_{OH} in the opposite sense from the rest of the terms.

Analysis of other combinations of parameters related to OHMs and their hosts does not reveal any new information or trends. In general, the observation errors are small compared to the scatter in any given parameter. The residuals in L_{OH} are always among the most difficult to reduce through projections onto principal axes, indicating that there are hidden variables influencing the properties of OHMs. This is hardly surprising, given the size scales of most of the properties we measure compared to the size scales of masing. Factors likely to affect L_{OH} include beaming, saturation state(s), and collisional pumping.

6. CONCLUSIONS

All of these analyses are folded into a new understanding of the OH megamaser phenomenon which unfortunately tends to reject the conventional wisdom about OHM environments and production mechanisms without offering a clean new picture. Most of the difficulty with constructing a model for OHM production lies in the large scatter intrinsic to the masing amplification process which relies on small scale conditions found in largely unresolved sources. OHMs show significant intrinsic variation in properties, producing intrinsic scatter roughly equal to the span of the sample data. Higher resolution imaging and spectroscopy in the radio, optical, and infrared bands offers some promise for placing the OHMs in the context of a merging systems and relating OHM activity to the stage and activity level of major galaxy mergers. Paper V touches on a few of these issues and points towards fairly short lifetimes for OHMs: certainly less than 10^8 years and more likely less than 10^7 years.

We have demonstrated the ability to identify OHM candidates with much success by selecting systems with high L_{FIR} . FIR-selected candidates at $z > 0.1$ conspire with the increasing OHM fraction versus L_{FIR} to produce a

StatLib⁶, a service hosted by Carnegie Mellon University. Table 9 presents the results of the principal component

⁶ <http://lib.stat.cmu.edu>

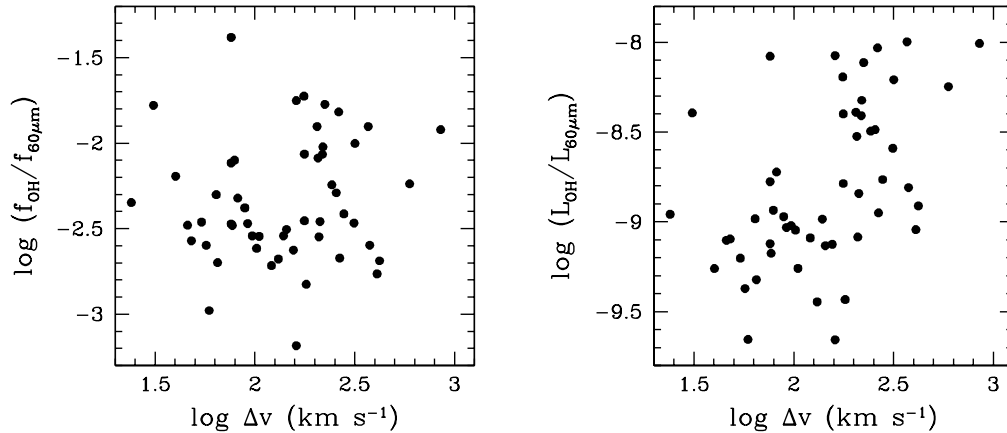


FIG. 14.— OH pumping efficiency versus line width. Two measures of OH pumping efficiency are plotted: the ratio of the peak OH flux density to the $60\ \mu\text{m}$ flux density, and the ratio of the OH line luminosity to the $60\ \mu\text{m}$ luminosity. Both measures show poor correlation with OH line width, unlike the result obtained by Staveley-Smith *et al.* (1992) which shows an anticorrelation (narrower OH lines have higher gain).

high detection rate (1 in 5.5), doubling the sample of OHMs overall, and increasing the sample at $z > 0.1$ sevenfold. The survey detections are incorporated into a reliable OH luminosity function and projected to high redshift for various merger evolution scenarios in Paper IV. It is likely that OH gigamasers (if they exist) may be detected out to $z = 5$ with future instrumentation, and can serve as luminous radio tracers of merging systems, dust-obscured star formation, and the formation of binary supermassive black holes.

Incorporating all reliable OHM detections, we reexamine the OH-FIR relationship and find: $L_{OH} \propto L_{FIR}^{1.2 \pm 0.1}$. This may indicate a mixture of saturation states across the sample or within individual merging systems. It is likely that cases of mostly saturated and mostly unsaturated masing are in the Arecibo OHM sample, but spatially resolved spectral line maps would be required to confirm our suspicions about individual systems.

Significant trends between properties of OHMs and their hosts or between OHM line properties are few. There is generally a mismatch of size scales between masing, which amplifies small-scale conditions, and properties of mostly unresolved merging systems, which represent integrated global quantities. The trend of increasing OHM fraction with increasing L_{FIR} and warmer FIR colors indicates that global properties of merging systems can indicate the likelihood that a given merging system will host the environments which produce OHMs, but these global properties cannot predict the nature of the OHM which is produced due to the amplification of small-scale conditions.

The most luminous OHMs tend to be not only strong (with a high observed flux density) but broad, spanning more than $1000\ \text{km s}^{-1}$ at 10% of peak flux density. The two OH gigamasers detected by this survey (*IRAS* F12032+1707 and F14070+0525) show multiple strong OH line components and are produced in two of the most luminous ULIRGs in the survey sample.

The authors are very grateful to Will Saunders for access to the PSCz catalog and to the excellent staff of NAIC for observing assistance and support. We thank the anonymous referees for insightful comments and constructive criticism. This research was supported by Space

Science Institute archival grant 8373 and NSF grant AST 00-98526 and made use of the NASA/IPAC Extragalactic Database (NED) which is operated by the Jet Propulsion Laboratory, California Institute of Technology, under contract with the National Aeronautics and Space Administration. We acknowledge the use of NASA's SkyView facility (<http://skyview.gsfc.nasa.gov>) located at NASA Goddard Space Flight Center.

REFERENCES

- Baan, W. A. 1989, *ApJ*, 338, 804
 Baan, W. A. 1991, in *ASP Conf. Ser. 16, Atoms, Ions, & Molecules: New Results in Spectral Line Astrophysics* (San Francisco: ASP), 45
 Baan, W. A., Rhoads, J., Fisher, K., Altschuler, D. R., & Haschick, A. 1992, *ApJ*, 396, 99
 Baan, W. A., Haschick, A., & Henkel, C. 1992, *AJ*, 103, 728
 Baan, W. A., Salzer, J. J., & LeWinter, R. D. 1998, *ApJ*, 509, 633
 Beers, T. C., Kriessler, J. R., Bird, C. M., & Huchra, J. P. 1995, *AJ*, 109, 874
 Beichman, C. A., Soifer, B. T., Helou, G., Chester, T. J., Neugebauer, G., Gillett, F. C., & Low, F. J. 1986, *ApJ*, 308, L1
 Bottinelli, L., Gougouenheim, L., Le Squeren, A. M., Dennefeld, M., & Paturel, G. 1985, *IAU Circ. No. 4106*
 Bottinelli, L., Gougouenheim, L., Le Squeren, A. M., Martin, J. M., Dennefeld, M., & Paturel, G. 1986, *IAU Circ. No. 4231*
 Bottinelli, L., Gougouenheim, L., Le Squeren, A. M., Martin, J. M., Dennefeld, M., & Paturel, G. 1987, *IAU Circ. No. 4357*
 Bottinelli, L., Gougouenheim, L., Le Squeren, A. M., Dennefeld, M., Martin, J. M., & Paturel, G. 1989, *IAU Circ. No. 4928*
 Bottinelli, L., Gougouenheim, L., Le Squeren, A. M., Martin, J. M., & Paturel, G. 1990, *IAU Circ. No. 4977*
 Boyce, P. J., Disney, M. J., Blades, J. C., Bokserberg, A., Crane, P., Deharveng, J. M., Macchetto, F. D., Mackay, C. D., & Sparks, W. B. 1996, *ApJ*, 473, 760
 Briggs, F. H. 1998, *A&A*, 336, 815
 Burdzyuzha, V. V. & Komberg, B. V. 1990, *A&A*, 234, 40
 Carilli, C. L., Wrobel, J. M., & Ulvestad, J. S. 1998, *AJ*, 115, 928
 Clements, D. L., Sutherland, W. J., McMahon, R. G., & Saunders, W. 1996, *MNRAS*, 279, 477
 Clowes, R. G., Campusano, L. E., Leggett, S. K., & Savage, A. 1995, *MNRAS*, 275, 819
 Condon, J. J., Anderson, M. L., & Helou, G. 1991, *ApJ*, 376, 95
 Condon, J. J., Cotton, W. D., Greisen, E. W., Yin, Q. F., Perley, R. A., Taylor, G. B., & Broderick, J. J. 1998, *AJ*, 115, 1693
 de Vaucouleurs, G., de Vaucouleurs, A., Corwin Jr., H. G., Buta, R. J., Paturel, G., & Fouque, P. 1991, *Third Reference Catalogue of Bright Galaxies* V. 3.9
 Darling, J. & Giovanelli, R. 2000, *AJ*, 119, 3003 (Paper I)
 Darling, J. & Giovanelli, R. 2001, *AJ*, 121, 1278 (Paper II)
 Darling, J. & Giovanelli, R. 2002a, *ApJ*, in press (Paper IV)
 Darling, J. & Giovanelli, R. 2002b, *AJ*, in preparation (Paper V)

- Dey, A., Strauss, M. A., & Huchra, J. 1990, AJ, 99, 463
- Diamond, P. J., Lonsdale, C. J., Lonsdale, C. J., & Smith, H. E. 1999, ApJ, 511, 178
- Dickey, J. M., Planesas, P., Mirabel, I. F., & Kazes, I. 1990, AJ, 100, 1457
- Downes, D., Solomon, P. M., & Radford, S. J. E. 1993, ApJ, 414, L13
- Duc, P.-A., Mirabel, I. F., & Maza, J. 1997, A&AS, 124, 533
- Feigelson, E. D. & Nelson, P. I. 1985, ApJ, 293, 192
- Fisher, K. B., Huchra, J. P., Strauss, M. A., Davis, M., Yahil, A., & Schlegel, D. 1995, ApJS, 100, 69
- Fullmer, L. & Lonsdale, C. 1989, *Cataloged Galaxies and Quasars observed in the IRAS Survey*, Jet Propulsion Laboratory, Pasadena, California.
- Giovanelli, R. & Haynes, M. P. 1993, AJ, 105, 1271
- Grogan, N. A. & Geller, M. J. 2000, AJ, 119, 32
- Haynes, M. P., Giovanelli, R., Herter, T., Vogt, N. P., Freudling, W., Maia, M. A. G., Salzer, J. J., & Wegner, G. 1997, AJ, 113, 1197
- Henkel, C., Güsten, R., & Baan, W. A. 1987, A&A, 185, 14
- Henkel, C. & Wilson, T. L. 1990, A&A, 229, 431
- Huchra, J., Davis, M., Latham, D., & Tonry, J. 1983, ApJS, 52, 89
- Huchra, J. P., Vogeley, M. S., & Geller, M. J. 1999, ApJS, 121, 287
- Kandalian, R. A. 1996, *Astrophysics*, 39, 237
- Kartgert, P., Mazure, A., den Hartog, R., Adami, C., Biviano, A., & Perea J. 1998, A&AS, 129, 399
- Kazes, I., Mirabel, I. F., & Combes, F. 1988, IAU Circ. No. 4629
- Kazes, I., Mirabel, I. F., & Combes, F. 1989, IAU Circ. No. 4856
- Kazes, I. & Baan, W. A. 1991, A&A, 248, 15
- Kim, D.-C., Sanders, D. B., Veilleux, S., Mazzarella, J. M., & Soifer, B. T. 1995, ApJS, 98, 129
- Kim, D.-C. & Sanders, D. B. 1998, ApJS, 119, 41
- Kim, D.-C., Veilleux, S., & Sanders, D. B. 1998, ApJ, 508, 627
- Klaas, U. & Elsässer, H. 1991, A&AS, 90, 33
- LaValley, M., Isobe, T., & Feigelson, E. D. 1992, BAAS, 24, 839
- Lawrence, A., et al. 1999, MNRAS, 308, 897
- Leech, K. J., Rowan-Robinson, M., Lawrence, A., & Hughes, J. D. 1994, MNRAS, 267, 253
- Lineweaver, C. H., Tenorio, L., Smoot, G. F., Keegstra, P., Banday, A. J., & Lubin, P. 1996, ApJ, 470, 38
- Lo, K.-Y., Chen, H.-W., & Ho, P. T. P. 1999, A&A, 341, 348
- Low, F. J., Cutri, R. M., Huchra, J. P., & Kleinmann, S. G. 1988, ApJ, 327, L41
- Lu, N. Y. & Freudling, W. 1995, ApJ, 449, 527
- Lutz, D., Veilleux, S., & Genzel, R. 1999, ApJ, 517, L13
- Martin, J. M., Le Squeren, A. M., Bottinelli, L., Gougouenheim, L., & Dennefeld, M. 1988, A&A, 201, L13
- Mirabel, I. F. & Sanders, D. B. 1987, ApJ, 322, 688
- Moran, E. C., Halpern, J. P., & Helfand, D. J. 1996, ApJS, 106, 341
- Murphy, T. W., Jr., Armus, L., Matthews, K., Soifer, B. T., Mazzarella, J. M., Shupe, D. L., Strauss, M. A., & Neugebauer, G. 1996, AJ, 111, 1025
- Murtagh, F. & Heck, A. 1987, *Multivariate Data Analysis*, Kluwer Academic, Dordrecht
- Nakanishi, K., Takata, T., Yamada, T., Takeuchi, T. T., Shiroya, R., Miyazawa, M., Watanabe, S., & Saito, M. 1997, ApJS, 112, 245
- Nordgren, T. E., Chengalur, J. N., Salpeter, E. E., & Terzian, Y. 1997, AJ, 114, 77
- Richter, O.-G. & Huchtmeir, W. K. 1987, A&AS, 68, 427
- Sanders, D. B., Soifer, B. T., Elias, J. H., Neugebauer, G., & Matthews, K. 1988, ApJ, 328, L35
- Sanders, D. B., Egami, E., Lipari, S., Mirabel, I. F., & Soifer, B. T. 1995, AJ, 110, 1993
- Sanders, D. B., Surace, J. A., & Ishida, C. M. 1999, in IAU Symp. 186, *Galaxy Interactions at Low and High Redshift*, ed. D. B. Sanders & J. Barnes (Dordrecht: Kluwer), 289
- Saunders, W., et al. 2000, MNRAS, 317, 55
- Scoville, N. Z., Evans, A. S., Thompson, R., Rieke, M., Hines, D. C., Low, F. J., Dinshaw, N., Surace, J. A., & Armus, L. 2000, AJ, 119, 991
- Skinner, C. J., Smith, H. A., Sturm, E., Barlow, M. J., Cohen, R. J., & Stacey, G. J. 1997, Nature, 386, 472
- Smith, B. J., Kleinmann, S. G., Huchra, J. P., & Low, F. J. 1987, ApJ, 318, 161
- Smith, H. E., Lonsdale, C. J., & Lonsdale, C. J. 1998, ApJ, 492, 137
- Solomon, P. M., Downes, D., Radford, S. J. E., & Barrett, J. W. 1997, ApJ, 478, 144
- Spinrad, H., Marr, J., Aguilar, L., Djorgovski, S. 1985, PASP, 97, 932
- Staveley-Smith, L., Unger, S. W., Cohen, R. J., Chapman, J. M. & Pointon, L. 1986, IAU Circ. No. 4248
- Staveley-Smith, L., Cohen, R. J., Chapman, J. M., Pointon, L., & Unger, S. W. 1987, MNRAS, 226, 689
- Staveley-Smith, L., Norris, R. P., Chapman, J. M., Allen, D. A., Whiteoak, J. B., & Roy, A. L. 1992, MNRAS, 258, 725
- Strauss, M. A., & Huchra, J. 1988, AJ, 95, 1602
- Strauss, M. A., Huchra, J. P., Davis, M., Yahil, A., Fisher, K. B., & Tonry, J. 1992, ApJS, 83, 29
- Szomoru, A., van Gorkom, J. H., & Gregg, M. D. 1996, AJ, 111, 2141
- Theureau, G., Bottinelli, L., Coudreau-Durand, N., Gougouenheim, L., Hallet, N., Loulégue, M., Paturol, G., & Teerikorpi, P. 1998, A&AS, 130, 333
- Unger, S. W., Chapman, J. M., Cohen, R. J., Hawarden, T. G., & Mountain, C. M. 1986, MNRAS, 220, 1P
- Veilleux, S., Kim, D.-C., Sanders, D. B., Mazzarella, J. M., & Soifer, B. T. 1995, ApJS, 98, 171
- Veilleux, S., Sanders, D. B., & Kim, D.-C. 1997, ApJ, 484, 92
- Veilleux, S., Kim, D.-C., & Sanders, D. B. 1999, ApJ, 522, 113
- White, R. L. et al. 2000, ApJS, 126, 133
- Wilman, R. J., Fabian, A. C., Cutri, R. M., Crawford, C. S., & Brandt, W. N. 1998, MNRAS, 300, L7
- Wu, H., Zou, Z. L., Xia, X. Y., & Deng, Z. G. 1998, A&AS, 132, 181
- Yun, M. S., Reddy, N. A., & Condon, J. J. 2001, ApJ, 554, 803

TABLE 1—*Continued*

<i>IRAS</i> Name	α	δ	z_{\odot}	Ref	v_{\odot}	v_{CMB}	D_L	f_{60}	f_{100}	$\log L_{FIR}$
FSC	B1950	B1950			km/s	km/s	h_{75}^{-1} Mpc	Jy	Jy	$h_{75}^{-2} L_{\odot}$
(1)	(2)	(3)	(4)	(5)	(6)	(7)	(8)	(9)	(10)	(11)
18065+3117	18 06 31.8	+31 17 49	0.1153	1	34580(132)	34480(136)	486(2)	0.608(42)	< 1.17	11.17–11.41
18286+2808	18 28 38.6	+28 08 26	0.1048	1	31429(103)	31299(108)	439(2)	0.696(90)	< 5.19	11.14–11.73
18407+3558	18 40 42.2	+35 58 12	0.1039	1	31159(106)	31018(111)	435(2)	0.669(40)	2.15(15)	11.46
23152+1318	23 15 15.8	+13 18 41	0.1075	1	32238(123)	31872(123)	448(2)	0.562(62)	< 0.93	11.06–11.28
23317+1141	23 31 48.0	+11 41 31	0.1197	1	35896(109)	35530(109)	502(2)	0.933(75)	< 2.44	11.38–11.68

REFERENCES.—Redshifts were obtained from: (1) Saunders *et al.* 2000; (2) Lawrence *et al.* 1999; (3) Klaas & Elsässer 1991; (4) Huchra *et al.* 1983; (5) Fisher *et al.* 1995; (6) Kim & Sanders 1998; (7) Clowes *et al.* 1995; (8) Leech *et al.* 1994; (9) Kim *et al.* 1995; (10) Downes, Solomon, & Radford 1993; (11) Strauss & Huchra 1988; (12) Beers *et al.* 1995; (13) Dey, Strauss, & Huchra 1990.

TABLE 2
OH NON-DETECTIONS: OH LIMITS AND 1.4 GHz PROPERTIES

IRAS Name FSC (1)	z_{\odot} (2)	$\log L_{FIR}$ $h_{75}^{-2}L_{\odot}$ (3)	$\log L_{OH}^{pred}$ $h_{75}^{-2}L_{\odot}$ (4)	$\log L_{OH}^{max}$ $h_{75}^{-2}L_{\odot}$ (5)	t_{on} min (6)	RMS mJy (7)	$f_{1.4GHz}^a$ mJy (8)	Class ^b (9)	Note (10)
00020+3636	0.1179	11.49	1.83	1.80	12	0.74	15.4(1.4)		
00085+3107	0.1025	11.28	1.55	1.52	12	0.51	< 5.0		
00109+0228	0.1590	11.74	2.18	2.02	12	0.67	< 5.0		
00128+2817	0.1405	11.63	2.03	1.84	16	0.56	4.9(0.5)		
00268+2413	0.1094	11.58	1.95	1.45	40	0.38	6.6(0.5)		
00310+1437	0.1154	11.58	1.96	1.65	12	0.54	< 5.0		1
00331+2656	0.1923	11.96	2.49	2.20	12	0.68	8.5(0.6)	L(1)	
00486+0004	0.1127	11.35	1.64	1.73	12	0.69	< 5.0		2
00507+0426	0.1009	11.18	1.41	1.51	12	0.52	5.4(0.6)		2
00523+1643	0.1385	11.55	1.92	1.84	12	0.58	< 5.0		
01097+2733	0.1304	11.57	1.94	1.79	12	0.58	3.7(0.5)		
01185+2547	0.1845	11.67–11.89	2.08–2.38	2.08	20	0.57	4.1(0.5)		
01208+3525	0.1108	11.35	1.64	1.72	12	0.69	3.2(0.5)	H(1)	2
01236+3504	0.1341	11.59	1.98	1.93	12	0.76	6.9(0.5)	S2(1)	
01411+1551	0.1040	11.00–11.44	1.16–1.77	1.50	12	0.47	< 5.0		2
01478+1254	0.1470	11.28–11.69	1.55–2.11	1.85	12	0.53	< 5.0		2
01572+0009	0.1630	12.19	2.80	2.08	12	0.73	26.7(0.9)	S1(2)	
02072+2336	0.1104	11.48	1.82	1.58	12	0.50	10.6(0.6)		
02077+2255	0.1005	11.47	1.81	1.54	12	0.55	5.9(0.5)		3
02124+2550	0.1219	11.45	1.77	1.67	12	0.51	6.9(0.5)		
02173+2143	0.1034	11.04–11.41	1.22–1.72	1.53	12	0.51	5.0(0.5)		2
02183+2254	0.1512	11.83	2.30	1.94	12	0.61	7.2(0.5)		
02323+0626	0.1266	11.47–11.70	1.81–2.12	1.75	12	0.57	3.2(0.5)		
02354+1926	0.1404	11.64	2.05	1.90	12	0.65	6.4(0.5)		
02411+0353	0.1436	11.91	2.42	1.89	12	0.60	6.9(0.5)	H(3)	
02459+2236	0.1631	11.44–11.92	1.77–2.43	1.98	12	0.58	< 5.0		2
02477+2654	0.1151	11.59	1.98	1.71	12	0.63	6.2(0.5)		
02488+3542	0.1108	11.09–11.43	1.28–1.76	1.69	12	0.65	< 5.0		2
04137+1217	0.2030	12.37	3.05	2.19	12	0.60	11.4(0.6)	L(1)	
04413+2608	0.1712	11.66–11.98	2.08–2.51	2.04	12	0.59	< 5.0	S2(4)	4
05324+0252	0.1533	11.47–11.79	1.81–2.25	1.61	60	0.28	4.2(0.5)		
05559+1020	0.1684	11.67–11.93	2.08–2.45	2.00	16	0.56	< 5.0		1
08206+3111	0.1503	11.63	2.03	2.04	12	0.77	7.9(0.5)		2
08232+0058	0.2429	12.03	2.59	2.38	16	0.64	3.7(0.6)		
11434+0159	0.1060	11.33	1.62	1.62	12	0.58	< 5.0		
11511+0946	0.1388	11.57	1.94	1.92	12	0.67	< 5.0		
11582+3020	0.2230	12.24	2.87	2.45	12	0.89	3.4(0.5)	L(5)	
12461+0416	0.1066	11.25	1.50	1.64	12	0.59	5.2(0.6)		2
12468+3436	0.1192	11.62	2.02	1.83	12	0.74	5.0(0.5)		
12491+0811	0.1081	11.36	1.65	1.59	12	0.52	< 5.0		
12514+1027	0.3189	12.35	3.03	2.45	24	0.43	8.7(0.5)	S2(6)	
12526+1025	0.1090	11.33	1.61	1.63	12	0.56	3.3(0.5)		2
12551+0825	0.2699	11.96–12.14	2.48–2.73	2.38	16	0.51	7.3(0.6)		
12569+3135	0.1021	11.23	1.48	1.54	24	0.52	3.2(0.5)		2
13034+0017	0.1371	11.51	1.86	1.96	12	0.76	9.9(0.6)		2.5
13064+2057	0.1142	11.48	1.83	1.69	12	0.59	10.7(0.6)		
13065+0449	0.2227	11.80–12.01	2.26–2.55	2.28	16	0.60	6.3(0.5)		2
13145+2356	0.1380	11.69	2.11	1.92	12	0.78	13.6(0.6)		
13156+0435	0.1133	11.64	2.04	1.68	12	0.59	11.5(0.6)		
13163+3209	0.1288	11.44	1.77	1.92	12	0.78	4.1(0.5)		2
13180+0133	0.1037	11.35	1.65	1.60	12	0.57	7.4(1.1)		
13243+2042	0.1340	11.54	1.90	1.86	12	0.64	4.2(0.5)		
13349+2438	0.1076	11.12–11.33	1.32–1.61	1.69	12	0.66	20.0(0.8)	S1(7)	2,6
13442+2321	0.1421	11.98	2.51	1.95	12	0.70	2.8(0.5)		
13443+0802	0.1353	11.85	2.33	1.83	12	0.57	10.8(0.6)	S2(3)	
13446+1623	0.2138	12.08	2.65	2.28	12	0.66	< 5.0		
13447+2833	0.2552	12.22	2.85	2.49	12	0.74	8.3(0.5)		
13457+3513	0.1156	11.56	1.93	1.77	12	0.70	< 5.0		
13478+1643	0.1124	11.30	1.57	1.67	12	0.58	7.1(0.5)		2
14020+1036	0.1022	11.32	1.61	1.54	12	0.52	3.7(0.6)		
14041+0117	0.2367	12.01–12.15	2.56–2.74	2.48	8	0.84	15.1(0.7)	S2(8)	
14111+1819	0.1115	11.40	1.71	1.68	12	0.60	4.0(0.6)		
14183+0009	0.1022	11.30	1.57	1.59	12	0.59	6.8(0.5)		2
14197+0813	0.1310	11.75	2.20	1.72	20	0.48	3.8(0.5)		7
14219+2009	0.1084	11.12–11.34	1.32–1.62	1.52	36	0.45	< 5.0		2
14312+2825	0.1749	11.90	2.40	2.07	12	0.60	6.1(0.5)	S2(1,9)	
14459+1745	0.1538	11.79	2.25	1.97	16	0.62	< 5.0		
14469+1402	0.1039	11.41	1.73	1.58	16	0.55	7.6(0.5)		
14488+3521	0.2058	11.97	2.50	2.27	15	0.69	6.7(0.5)	H(1)	1,8
14550+0715	0.1398	11.65	2.06	1.91	12	0.65	5.8(0.6)		7
15069+1808	0.1706	11.79	2.25	2.08	12	0.64	12.1(0.6)	S1(10)	
15165+1553	0.1194	11.35	1.65	1.72	20	0.58	< 5.0		2,7
15563+1233	0.2038	11.95	2.47	2.24	12	0.65	4.2(0.5)	L(1)	
16075+0059	0.1187	11.12–11.53	1.33–1.89	1.73	12	0.61	3.6(0.6)		2
16142+0321	0.1059	11.53	1.88	1.59	12	0.55	9.6(1.1)		
16523+3126	0.1027	11.20–11.37	1.44–1.66	1.64	12	0.66	< 5.0		2
16525+3322	0.1354	11.43–11.67	1.75–2.09	1.93	12	0.73	3.8(0.5)	H(11)	2
17225+0256	0.1116	11.30–11.58	1.57–1.95	1.59	16	0.50	4.1(0.5)		2,7
17481+2135	0.1166	11.18–11.54	1.41–1.91	1.78	12	0.71	5.2(0.5)		2
17546+1356	0.1205	11.30–11.53	1.58–1.89	1.57	20	0.41	8.9(0.5)		7

TABLE 2—Continued

IRAS Name	z_{\odot}	$\log L_{FIR}$	$\log L_{OH}^{pred}$	$\log L_{OH}^{max}$	t_{on}	RMS	$f_{1.4GHz}^a$	Class ^b	Note
FSC (1)	(2)	$h_{75}^{-2}L_{\odot}$ (3)	$h_{75}^{-2}L_{\odot}$ (4)	$h_{75}^{-2}L_{\odot}$ (5)	min (6)	mJy (7)	mJy (8)	(9)	(10)
18065+3117	0.1153	11.17–11.41	1.39–1.72	1.70	12	0.60	< 5.0		2,7
18286+2808	0.1048	11.14–11.73	1.35–2.16	1.58	12	0.55	4.4(0.5)		2
18407+3558	0.1039	11.46	1.80	1.63	12	0.63	6.8(0.5)		
23152+1318	0.1075	11.06–11.28	1.24–1.54	1.48	12	0.42	< 5.0		2
23317+1141	0.1197	11.38–11.68	1.68–2.10	1.62	12	0.47	4.0(0.5)		

^a1.4 GHz continuum fluxes are courtesy of the NRAO VLA Sky Survey (Condon *et al.* 1998).

^bSpectral classifications use the codes: “S2” = Seyfert type 2; “S1” = Seyfert type 1; “H” = HII region (starburst); and “L” = low-ionization emission region (LINER).

REFERENCES.—Spectral classifications were obtained from: (1) Darling & Giovanelli 2002b (Paper V); (2) Wu *et al.* 1998; (3) Veilleux, Kim, & Sanders 1999; (4) Lawrence *et al.* 1999; (5) Kim, Veilleux, & Sanders 1998; (6) Wilman *et al.* 1998; (7) Veilleux *et al.* 1995; (8) Clowes *et al.* 1995; (9) Leech *et al.* 1994; (10) Moran, Halpern, & Helfand 1996; (11) White *et al.* 2000.

NOTE.— (1) Source needs more integration time, due to a suggestive feature in the bandpass; (2) Source needs more integration time, based on $L_{OH}^{pred} < L_{OH}^{max}$; (3) Lu & Freudling (1995) list an HI redshift and spectrum with $z = 0.04714$ which is not unambiguous, but casts doubt on the PSCz redshift of this source; (4) Galactic HII in bandpass; (5) Possible OH absorption feature, but $\lesssim 1$ mJy deep; (6) Radio quiet IR QSO (Beichman *et al.* 1986); (7) Observations were performed during daylight, which increases the RMS noise significantly; (8) Possible 2–3 mJy OH emission feature 220 km s^{-1} redward of the optical redshift.

TABLE 3
AMBIGUOUS CANDIDATES: OPTICAL REDSHIFTS AND FIR PROPERTIES

IRAS Name	α	δ	z_{\odot}	Ref	v_{\odot}	v_{CMB}	D_L	$f_{60\mu m}$	$f_{100\mu m}$	$\log L_{FIR}$	Note
FSC (1)	B1950 (2)	B1950 (3)	(4)	z (5)	km/s (6)	km/s (7)	h_{75}^{-1} Mpc (8)	Jy (9)	Jy (10)	$h_{75}^{-2}L_{\odot}$ (11)	(12)
00242+3344	00 24 14.9	+33 44 51	0.1737	1	52067(135)	51754(137)	750(2)	0.601(84)	1.33(23)	11.81	1
00302+3625	00 30 17.7	+36 25 26	0.3023	1	90628(159)	90325(161)	1386(3)	0.682(61)	0.77(17)	12.28	2
01348+3254	01 34 48.8	+32 54 07	0.3670	2	110024()	109752(27)	1731(0)	0.740(52)	< 1.15	12.36–12.56	3,4
01506+2554	01 50 39.2	+25 54 54	0.3264	1	97855(381)	97584(382)	1513(7)	0.578(52)	1.14(21)	12.38	2
02054+0835	02 05 27.5	+08 35 54	0.3450	3	103428(250)	103161(251)	1612(5)	0.561(67)	< 1.99	12.17–12.55	2
06587+3043	06 58 47.8	+30 43 42	0.1727	1	51788(121)	51910(127)	752(2)	0.673(74)	< 1.98	11.59–11.92	1
07488+0501	07 48 52.4	+05 01 17	0.1732	1	51935(129)	52165(132)	756(2)	0.661(53)	1.18(11)	11.82	1
08519+2017	08 51 58.9	+20 17 57	0.3060	1	91738()	92006(27)	1415(0)	0.891(62)	1.16(23)	12.44	2,3
10579+0438	10 57 59.3	+04 38 06	0.1734	3	51984(250)	52345(250)	759(4)	0.648(65)	0.99(21)	11.78	1
12265+0219	12 26 32.6	+02 19 46	0.1583	4	47469(20)	47812(24)	688(0)	2.060(144)	2.89(228)	12.19	3,5
12266+3240	12 26 38.3	+32 40 53	0.1742	1	52225(300)	52492(301)	761(5)	0.572(63)	0.76(14)	11.71	1
13014+3524	13 01 31.2	+35 24 36	0.2379	5	71328(300)	71565(301)	1068(5)	0.564(62)	0.74(13)	12.00	6
13380+3339	13 37 58.9	+33 39 51	0.2499	1	74925(600)	75143(601)	1127(10)	0.940(66)	1.10(14)	12.25	2
13451+1232 ^a	13 45 06.5	+12 32 21	0.1212	1	36341(300)	36609(301)	518(5)	1.916(211)	2.06(20)	11.87	3,7
15438+0438	15 43 52.0	+04 38 30	0.2370	1	71046()	71175(34)	1062(1)	0.783(55)	1.02(26)	12.13	2
16280+0531	16 28 06.2	+05 31 22	0.1738	1	52103(141)	52164(146)	756(2)	0.636(51)	< 0.90	11.57–11.76	1
17281+3120	17 28 10.3	+31 20 30	0.2374	1	71164(191)	71115(194)	1061(3)	0.593(42)	0.97(25)	12.05	2
17491+1531	17 49 11.1	+15 31 12	0.1737	1	52070(108)	51997(114)	753(2)	0.604(66)	1.81(20)	11.88	1
20551+2441	20 55 07.7	+24 41 59	0.2425	6	72702(199)	72406(200)	1082(3)	1.056(84)	1.44(13)	12.29	2
23060+0505	23 06 00.9	+05 05 08	0.1729	1	51847(48)	51479(48)	745(1)	1.152(81)	0.83(17)	11.92	1
23113+0314	23 11 21.4	+03 14 37	0.3053	1	91539(199)	91171(199)	1400(3)	1.217(85)	1.27(18)	12.53	2
23140+0348	23 14 02.2	+03 48 58	0.2198	1	65890()	65522(3)	969(0)	0.602(60)	0.79(19)	11.94	3,8
23219+2919	23 22 01.2	+29 19 20	0.2401	5	71980(300)	71640(300)	1069(5)	0.903(90)	< 2.03	12.02–12.30	2
23444+0441	23 44 26.5	+04 41 24	0.1723	1	51657(107)	51293(107)	742(2)	0.664(60)	1.54(29)	11.85	1
23539+2322	23 53 57.8	+23 22 10	0.2660	1	79754(144)	79407(145)	1199(2)	0.586(59)	< 1.19	11.93–12.19	2

^aThis marginal OH detection (3.4 σ ; Dickey *et al.* 1990) was undetectable at Arecibo due to standing waves produced by its strong continuum.

REFERENCES.—Redshifts were obtained from: (1) Saunders *et al.* 2000; (2) Spinrad *et al.* 1985; (3) Lawrence *et al.* 1999; (4) Strauss *et al.* 1992; (5) Leech *et al.* 1994; (6) Nakanishi *et al.* 1997.

NOTE.— (1) 1667 MHz OH line undetectable due to Galactic HII; (2) OH undetectable due to RFI; (3) Continuum creates standing waves, making OH undetectable; (4) 3C048; (5) 3C273; (6) Continuum source (444 mJy; Condon *et al.* 1998) 82'' from this target creates standing waves, making OH undetectable; (7) 4C12.50; (8) 3C459.

TABLE 4
 AMBIGUOUS CANDIDATES: 1.4 GHz PROPERTIES AND NOTES

IRAS Name FSC (1)	z_{\odot} (2)	$\log L_{FIR}$ $h_{75}^{-2} L_{\odot}$ (3)	$\log L_{OH}^{pred}$ $h_{75}^{-2} L_{\odot}$ (4)	$f_{1.4GHz}$ ^a mJy (5)	Class ^b (6)	Note (7)
00242+3344	0.1737	11.81	2.27	20.1(0.8)		1
00302+3625	0.3023	12.28	2.93	< 5.0		2
01348+3254	0.3670	12.36–12.56	3.03–3.31	16018(481)	Q	3,4
01506+2554	0.3264	12.38	3.06	40.3(1.6)		2
02054+0835	0.3450	12.17–12.55	2.78–3.30	10.5(1.2)	S1(1)	2
06587+3043	0.1727	11.59–11.92	1.97–2.43	6.8(0.5)		1
07488+0501	0.1732	11.82	2.29	3.4(0.5)		1
08519+2017	0.3060	12.44	3.14	1512.3(45.4)	Q	2,3
10579+0438	0.1734	11.78	2.24	< 5.0		1
12265+0219	0.1583	12.19	2.80	54992(1900)	Q	3,5
12266+3240	0.1742	11.71	2.14	3.0(0.5)		1
13014+3524	0.2379	12.00	2.53	< 5.0		6
13380+3339	0.2499	12.25	2.88	8.4(0.5)	S2(2)	2
13451+1232 ^c	0.1212	11.87	2.36	5398(162)	S2(3)	3,7
15438+0438	0.2370	12.13	2.72	5.0(0.5)		2
16280+0531	0.1738	11.57–11.76	1.95–2.21	< 5.0	L(4)	1
17281+3120	0.2374	12.05	2.61	4.8(0.5)		2
17491+1531	0.1737	11.88	2.37	< 5.0	L(4)	1
20551+2441	0.2425	12.29	2.93	14.7(0.6)		2
23060+0505	0.1729	11.92	2.43	6.8(0.5)	S2(5)	1
23113+0314	0.3053	12.53	3.28	47.6(1.5)		2
23140+0348	0.2198	11.94	2.46	4676(165)		3,8
23219+2919	0.2401	12.02–12.30	2.57–2.95	6.4(0.5)		2
23444+0441	0.1723	11.85	2.33	2.7(0.6)		1
23539+2322	0.2660	11.93–12.19	2.45–2.80	14.1(0.6)		2

^a1.4 GHz continuum fluxes are courtesy of the NRAO VLA Sky Survey (Condon *et al.* 1998).

^bSpectral classifications use the codes: “S2” = Seyfert type 2; “S1” = Seyfert type 1; “Q” = Quasar; and “L” = low-ionization emission region (LINER).

^cThis marginal OH detection (3.4σ ; Dickey *et al.* 1990) was undetectable at Arecibo due to standing waves produced by its strong continuum.

REFERENCES.—Spectral classifications were obtained from: (1) Lawrence *et al.* 1999; (2) Leech *et al.* 1994; (3) Kim, Veilleux, & Sanders 1998; (4) Darling & Giovanelli 2002b (Paper V); (5) Veilleux, Kim, & Sanders 1999.

NOTE.—(1) 1667 MHz OH line undetectable due to Galactic HI; (2) OH undetectable due to RFI; (3) Continuum creates standing waves, making OH undetectable; (4) 3C048; (5) 3C273; (6) Continuum source (444 mJy; Condon *et al.* 1998) $82''$ from this target creates standing waves, making OH undetectable; (7) 4C12.50; (8) 3C459.

TABLE 5
OH DETECTIONS: OPTICAL REDSHIFTS AND FIR PROPERTIES

<i>IRAS</i> Name FSC (1)	α B1950 (2)	δ B1950 (3)	z_{\odot} (4)	Ref z (5)	v_{\odot} km/s (6)	v_{CMB} km/s (7)	D_L h_{75}^{-1} Mpc (8)	$f_{60\mu m}$ Jy (9)	$f_{100\mu m}$ Jy (10)	$\log L_{FIR}$ $h_{75}^{-2} L_{\odot}$ (11)
01562+2528	01 56 12.0	+25 27 59	0.1658	1	49707(505)	49441(506)	714(8)	0.809(57)	1.62(24)	11.87
02524+2046	02 52 26.8	+20 46 54	0.1815	1	54421(125)	54213(129)	788(2)	0.958(77)	< 4.79	11.78–12.25
03521+0028	03 52 08.5	+00 28 21	0.1522	2	45622(138)	45501(142)	653(2)	2.638(237)	3.83(34)	12.25
03566+1647	03 56 37.8	+16 47 57	0.1335	1	40033(54)	39911(65)	568(1)	0.730(66)	< 2.37	11.38–11.73
10035+2740	10 03 36.7	+27 40 19	0.1662	1	49826(300)	50116(301)	724(5)	1.144(126)	1.63(161)	11.98
10378+1108 ^a	10 37 49.1	+11 09 08	0.1362	2	40843(61)	41190(62)	587(1)	2.281(137)	1.82(18)	12.02
11180+1623 ^b	11 18 06.7	+16 23 16	0.1660	3	49766(70)	50104(71)	724(1)	1.189(95)	1.60(18)	11.99
12005+0009	12 00 30.2	+00 09 24	0.1226	1	36759(177)	37116(177)	526(3)	0.736(88)	0.98(15)	11.50
12018+1941 ^a	12 01 51.8	+19 41 46	0.1686	4	50559(65)	50880(67)	736(1)	1.761(123)	1.78(23)	12.13
12162+1047	12 16 13.9	+10 47 58	0.1465	1	43931(149)	44267(150)	634(2)	0.725(58)	< 0.95	11.47–11.65
12549+2403	12 54 53.4	+24 03 57	0.1317	1	39491(145)	39772(147)	565(2)	0.739(66)	1.03(13)	11.57
13218+0552	13 21 48.4	+05 52 40	0.2051	4	61488(58)	61788(62)	909(1)	1.174(82)	0.71(14)	12.09
14043+0624	14 04 20.0	+06 24 48	0.1135	1	34025(114)	34283(117)	483(2)	0.795(64)	1.31(16)	11.49
14059+2000	14 05 56.4	+20 00 42	0.1237	1	37084(89)	37316(93)	529(1)	0.857(120)	1.88(32)	11.66
14070+0525 ^a	14 07 00.3	+05 25 40	0.2655	1	79591(400)	79847(401)	1206(7)	1.447(87)	1.82(18)	12.51
14553+1245	14 55 19.1	+12 45 21	0.1249	1	37449(133)	37636(136)	533(2)	0.888(53)	1.17(16)	11.59
14586+1432	14 58 41.6	+14 31 53	0.1477	1	44287(118)	44467(122)	637(2)	0.569(91)	1.07(17)	11.61
17161+2006	17 16 05.8	+20 06 04	0.1098	1	32928(113)	32903(118)	463(2)	0.632(44)	< 1.37	11.14–11.41
12107+3157 ^c	12 10 48.0	+31 57 36	0.2065	5	61907(300)	62183(301)	915(5)	0.987(108)	1.36(15)	12.11

^aA known OHM included in the survey sample.

^b*IRAS* 11180+1623 is not in the PSCz catalog (excluded by the PSCz mask; Saunders *et al.* 2000). It is in the 1 Jy survey (Kim & Sanders 1998).

^c*IRAS* 12107+3157 is an OH absorber.

REFERENCES.—Redshifts were obtained from: (1) Saunders *et al.* 2000; (2) Strauss *et al.* 1992; (3) Kim & Sanders 1998; (4) Fisher *et al.* 1995; (5) Lawrence *et al.* 1999.

TABLE 6
OH DETECTIONS: OH LINE AND 1.4 GHz CONTINUUM PROPERTIES

<i>IRAS</i> Name FSC (1)	$v_{1667,\odot}$ km/s (2)	t_{on} min (3)	f_{1667} mJy (4)	W_{1667} MHz (5)	Δv_{1667}^a MHz (6)	Δv_{1667}^b km/s (7)	R_H (8)	$\log L_{FIR}$ $h_{75}^{-2} L_{\odot}$ (9)	$\log L_{OH}^{pred}$ $h_{75}^{-2} L_{\odot}$ (10)	$\log L_{OH}$ $h_{75}^{-2} L_{\odot}$ (11)	$f_{1.4GHz}^c$ mJy (12)
01562+2528	49814(15)	32	6.95	1.29	1.04	218	5.9	11.87	2.37	3.22	6.3(0.5)
02524+2046	54162(15)	24	39.82	0.50	0.36	76	3.2	11.78–12.25	2.24–2.89	3.71	2.9(0.6)
03521+0028	45512(14)	72	2.77	0.61	0.29	59	5.8	12.25	2.89	2.41	6.7(0.6)
03566+1647	39865(14)	84	1.96	0.98	0.23	48	\gtrsim 9.6	11.38–11.73	1.69–2.17	2.29	3.5(0.5)
10035+2740	50065(14)	76	2.29	0.74	0.31	65	\gtrsim 15.4	11.98	2.51	2.47	6.3(0.5)
10378+1108 ^d	40811(14)	12	19.70	1.50	0.87	177	...	12.02	2.57	3.51	8.9(0.6)
11180+1623 ^e	49783(14)	48	1.82	0.42	0.61	127	\gtrsim 5.1	11.99	2.52	2.31	4.2(0.5)
12005+0009	36472(14)	40	3.51	0.71	0.41	82	\gtrsim 2.0	11.50	1.85	2.60	5.4(0.6)
12018+1941 ^d	50317(15)	16	2.63	0.81	0.86	181	\gtrsim 5.6	12.13	2.72	2.56	6.5(0.5)
12162+1047	43757(14)	60	2.07	0.64	0.51	105	\gtrsim 11.1	11.47–11.65	1.81–2.06	2.22	6.8(1.6)
12549+2403	39603(14)	68	1.79	0.89	0.50	102	\gtrsim 2.6	11.57	1.95	2.34	3.7(0.5)
13218+0552	61268(15)	60	4.01	2.49	1.45	314	...	12.09	2.66	3.41	5.3(0.5)
14043+0624	33912(14)	80	2.75	0.33	0.27	54	1.4	11.49	1.84	2.08	15.6(1.0)
14059+2000	37246(14)	28	15.20	1.10	0.80	161	5.3	11.66	2.06	3.32	7.5(0.5)
14070+0525 ^d	79929(16)	16	8.37	3.21	2.62	596	...	12.51	3.24	4.09	4.0(0.6)
14553+1245	37462(14)	56	2.93	0.39	0.38	77	\gtrsim 14.5	11.59	1.98	2.24	3.8(0.5)
14586+1432	44380(14)	16	7.11	\leq 2.67	1.79	369	...	11.61	2.00	3.38	11.1(0.6)
17161+2006	32762(14)	52	4.84	0.62	0.38	76	\sim 6.2	11.14–11.41	1.35–1.72	2.37	7.3(0.6)
12107+3157 ^f	61989(15)	16	-3.20	1.74	1.93	420	...	12.11	2.69	...	31.6(1.1)

^a Δv_{1667} is the *observed* FWHM.

^b Δv_{1667} is the *rest frame* FWHM. The rest frame and observed widths are related by $\Delta v_{rest} = c(1+z)(\Delta v_{obs}/v_{\odot})$.

^c1.4 GHz continuum fluxes are courtesy of the NRAO VLA Sky Survey ((Condon *et al.* 1998)).

^dRedetection of a known OHM included in the survey sample.

^e*IRAS* 11180+1623 is not in the PSCz catalog (excluded by the PSCz mask; Saunders *et al.* 2000). It is in the 1 Jy survey (Kim & Sanders 1998).

^f*IRAS* 12107+3157 is an OH absorber.

TABLE 7
KNOWN OH MEGASASERS: OPTICAL REDSHIFTS AND FIR PROPERTIES

Name	α	δ	z_{\odot}	Ref	v_{\odot}	v_{CMB}	D_L	f_{60}	f_{100}	$\log L_{FIR}$
FSC	J2000	J2000	(4)	(5)	km/s	km/s	h_{75}^{-1} Mpc	Jy	Jy	$h_{75}^{-2} L_{\odot}$
(1)	(2)	(3)			(6)	(7)	(8)	(9)	(10)	(11)
00057+4021	00 05 44.9	+40 21 15	0.0447	1	13389(9)	13090(24)	178(0)	4.47(0.36)	4.30(0.30)	11.30
00335-2732	00 33 32.0	-27 32 05	0.0693	2	20771(36)	20489(42)	283(1)	4.29(0.47)	3.21(0.22)	11.65
00509+1225	00 50 57.8	+12 25 20	0.0611	3	18330(20)	17997(26)	247(0)	2.24(0.18)	2.63(0.26)	11.31
01364-1042	01 36 24.3	-10 42 24	0.0484	4	14520(81)	14240(84)	194(1)	6.16(0.62)	6.70(0.54)	11.53
01417+1651	01 41 47.4	+16 51 02	0.0274	2	8245(5)	7956(25)	107(0)	12.55(1.00)	13.31(0.93)	11.32
02483+4302	02 48 19.8	+43 02 53	0.0514	1	15421(9)	15236(35)	208(0)	4.02(0.28)	6.92(0.41)	11.47
03056+2034	03 05 38.6	+20 34 54	0.0272	6	8164(36)	7972(49)	108(1)	4.41(0.26)	5.89(0.65)	10.90
03260-1422	03 26 04.6	-14 22 25	0.0425	2	12736(55)	12593(64)	171(1)	2.91(0.29)	4.84(0.34)	11.16
04332+0209	04 33 12.2	+02 09 24	0.0119	2	3580(55)	3521(66)	47(1)	3.38(0.20)	< 6.83	9.89-10.14
04454-4838	04 45 28.0	-48 38 54	0.0529	7	15862(30)	15870(45)	217(1)	5.69(0.23)	5.25(0.31)	11.57
05100-2425	05 10 04.9	-24 25 26	0.0335	2	10047(40)	10066(53)	136(1)	3.98(0.20)	5.14(0.21)	11.06
05414+5840	05 41 24.7	+58 40 52	0.0149	8	4455(9)	4443(39)	60(1)	14.45(0.72)	29.26(1.46)	10.97
06206-3646	06 20 40.2	-36 46 10	0.1080	2	32390(60)	32506(68)	457(1)	2.17(0.11)	2.54(0.28)	11.83
08071+0509	08 07 09.4	+05 09 56	0.0522	2	15650(42)	15901(51)	218(1)	4.50(0.27)	6.89(0.41)	11.54
09320+6134	09 32 04.8	+61 34 37	0.0394	1	11809(9)	11928(36)	162(0)	11.54(0.81)	20.23(1.01)	11.72
10038-3338	10 03 52.3	-33 38 24	0.0341	2	10223(36)	10540(40)	143(1)	8.90(0.71)	7.98(0.48)	11.40
10173+0829	10 17 22.0	+08 28 40	0.0480	2	14390(300)	14736(300)	201(4)	5.81(0.41)	5.47(0.44)	11.52
10378+1108	10 37 49.1	+11 09 08	0.1362	2	40843(61)	41190(62)	587(1)	2.28(0.14)	1.82(0.16)	12.02
10485-1447	10 48 35.3	-14 47 25	0.1330	9	39872(70)	40236(70)	572(1)	1.73(0.23)	1.66(0.30)	11.90
11011+4107	11 01 05.8	+41 07 11	0.0345	2	10350(27)	10596(38)	144(1)	5.84(0.35)	10.57(0.53)	11.32
11069+2711	11 06 56.9	+27 11 23	0.0703	10	21080(40)	21385(45)	295(1)	1.98(0.16)	4.08(0.24)	11.50
11257+5850	11 25 42.4	+58 50 17	0.0104	11	3121(3)	3272(32)	44(0)	103.7(6.2)	107.4(5.4)	11.46
11506-3851	11 50 39.9	-38 51 07	0.0108	12	3232(19)	3540(28)	47(0)	32.68(2.94)	41.62(2.50)	11.05
12018+1941	12 01 51.8	+19 41 46	0.1687	13	50559(65)	50880(67)	736(1)	1.76(0.12)	1.78(0.23)	12.13
12112+0305	12 11 12.5	+03 05 22	0.0730	9	21885(70)	22235(71)	307(1)	8.50(0.51)	9.98(0.80)	12.08
12243-0036	12 24 20.8	-00 36 04	0.0073	14	2179(8)	2525(15)	34(0)	40.68(3.66)	32.80(3.61)	10.79
12540+5708	12 54 05.0	+57 08 38	0.0422	15	12642(4)	12783(32)	174(0)	31.99(1.60)	30.29(1.21)	12.13
13097-1531	13 09 46.8	-15 31 57	0.0214	12	6400(31)	6717(37)	91(1)	11.13(0.67)	20.86(1.25)	11.21
13126+2453	13 12 39.5	+24 52 58	0.0112	16	3347(19)	3613(30)	48(0)	17.93(1.43)	18.13(1.09)	10.78
13254+4754	13 25 23.0	+47 54 53	0.0604	13	18107(179)	18277(181)	251(3)	1.89(0.13)	2.76(0.22)	11.28
13428+5608	13 42 51.7	+56 08 14	0.0378	1	11326(9)	11449(33)	156(0)	21.74(0.87)	21.38(0.86)	11.87
13451+1232	13 45 06.2	+12 32 20	0.1220	9	36575(70)	36843(74)	521(1)	1.92(0.21)	2.06(0.19)	11.88
14070+0525	14 07 00.5	+05 25 41	0.2644	1	79259(9)	79515(28)	1201(0)	1.45(0.09)	1.82(0.16)	12.50
15065-1107	15 06 32.8	-11 07 57	0.0063	12	1888(5)	2080(33)	28(0)	10.50(0.53)	19.67(0.79)	10.16
15107+0724	15 10 45.7	+07 24 37	0.0130	17	3897(28)	4071(43)	55(1)	20.76(1.04)	29.44(1.47)	10.99
15179+3956	15 17 55.8	+39 56 24	0.0476	18	14261(20)	14364(38)	196(1)	4.17(0.17)	3.07(0.15)	11.32
15233+0533	15 23 20.7	+05 33 14	0.0541	2	16227(24)	16385(41)	224(1)	3.49(0.31)	3.93(0.28)	11.41
15247-0945	15 24 43.6	-09 45 33	0.0400	2	11993(60)	12160(69)	165(1)	4.67(0.23)	5.99(0.42)	11.29
15250+3608	15 25 03.7	+36 09 01	0.0554	19	16602(53)	16706(62)	229(1)	7.29(0.36)	5.91(0.30)	11.71
15327+2340	15 32 46.9	+23 40 08	0.0181	12	5426(7)	5545(34)	75(0)	103.8(4.2)	112.4(3.4)	11.92
16145+4231	16 14 32.5	+42 31 18	0.0231	20	6944(15)	6978(37)	94(0)	1.30(0.06)	3.27(0.20)	10.37
16399-0937	16 39 55.7	-09 37 37	0.0270	2	8098(28)	8152(47)	110(1)	7.99(0.56)	12.52(1.13)	11.20
17207-0014	17 20 47.8	-00 14 15	0.0428	1	12834(9)	12816(39)	175(1)	31.14(1.87)	34.90(2.09)	12.14
17526+3253	17 52 39.1	+32 53 38	0.0260	12	7798(9)	7716(35)	104(0)	3.23(0.16)	7.35(0.29)	10.83
18544-3718	18 54 29.6	-37 18 41	0.0734	2	22012(57)	21910(68)	303(1)	2.84(0.26)	3.90(0.66)	11.61
20100-4156	20 10 05.8	-41 56 40	0.1296	2	38848(51)	38685(62)	549(1)	5.23(0.31)	5.17(0.36)	12.35
20491+1846	20 49 09.2	+18 46 50	0.0290	22	8716(7)	8418(22)	114(0)	2.79(0.14)	6.20(0.43)	10.84
20550+1655	20 55 04.2	+16 55 57	0.0361	23	10822(10)	10517(22)	143(0)	13.28(0.66)	10.57(0.74)	11.56
22025+4204	22 02 31.7	+42 05 02	0.0144	2	4323(31)	4033(37)	54(1)	9.69(0.58)	14.03(1.26)	10.66
22088-1831	22 08 49.8	-18 31 56	0.1702	13	51026(46)	50705(50)	733(1)	1.73(0.10)	1.73(0.16)	12.12
22491-1808	22 49 09.0	-18 08 20	0.0778	2	23312(22)	22979(27)	318(0)	5.44(0.38)	4.45(0.36)	11.87
23050+0359	23 05 01.3	+03 59 33	0.0474	2	14205(29)	13837(29)	189(0)	3.89(0.27)	5.30(0.32)	11.34
23135+2517	23 13 33.1	+25 17 01	0.0273	12	8197(6)	7847(13)	106(0)	9.76(0.98)	11.13(0.78)	11.21
23365+3604	23 36 32.2	+36 04 32	0.0645	1	19331(9)	19011(20)	262(0)	7.09(0.71)	8.36(0.50)	11.86

REFERENCES.—Redshifts were obtained from: (1) Downes, Solomon, & Radford 1993; (2) Strauss *et al.* 1992; (3) Solomon *et al.* 1997; (4) Kim *et al.* 1995; (6) Huchra, Vogeley, Geller 1999; (7) Sanders *et al.* 1995; (8) Theureau *et al.* 1998; (9) Kim & Sanders 1998; (10) Smith *et al.* 1987; (11) Nordgren *et al.* 1997; (12) de Vaucouleurs *et al.* 1991; (13) Fisher *et al.* 1995; (14) Richter & Huchtmeir 1987; (15) Carilli, Wrobel, & Ulvestad 1998; (16) Haynes *et al.* 1997; (17) Kartgert *et al.* 1998; (18) Szomoru, van Gorkom, & Gregg 1996; (19) Strauss & Huchra 1988; (20) Grogin & Geller 2000; (21) Reshetnikov & Combes 1994; (22) Saunders *et al.* 2000; (23) Giovanelli & Haynes 1993.

TABLE 8
KNOWN OH MEGAMASERS: OH AND 1.4 GHz PROPERTIES

IRAS Name FSC (1)	z_{\odot} (2)	$\log L_{FIR}$ $h_{75}^{-2} L_{\odot}$ (3)	$\log L_{OH}^{pred}$ $h_{75}^{-2} L_{\odot}$ (4)	$\log L_{OH}$ $h_{75}^{-2} L_{\odot}$ (5)	f_{1667} mJy (6)	Ref (7)	$f_{1.4GHz}^a$ mJy (8)	Class ^b (9)	Note (10)
00057+4021	0.0447	11.30	1.57	1.90	...	1	7.4(0.5)	S2(1)	2
00335-2732	0.0693	11.65	2.06	2.61	...	2	11.3(0.6)	C(1)	2
00509+1225	0.0611	11.31	1.59	1.78	...	2	8.8(0.6)	S1(2)	2
01364-1042	0.0484	11.53	1.89	2.00	...	3	15.8(0.7)	L(3,6)	2
01417+1651	0.0274	11.32	1.60	2.65	240	4	40.6(1.3)	L(1),H/L(3),H/A(4)	
02483+4302	0.0514	11.47	1.81	2.49	...	5	1225(36)	L(1)	2
03056+2034	0.0272	10.90	1.02	1.28	...	2	17.9(1.0)	H(1)	2
03260-1422	0.0425	11.16	1.38	1.99	...	5	11.4(0.6)	H(1)	2
04332+0209	0.0119	9.89-10.14	-(0.38-0.03)	0.44	8	6	4.3(0.5)	H(1)	2,3
04454-4838	0.0529	11.57	1.95	2.88	142	6	
05100-2425	0.0335	11.06	1.24	2.07	16	6	20.2(0.8)	L(1)	2
05414+5840	0.0149	10.97	1.12	0.80	4	7	137.8(4.9)	S2(1)	2,3
06206-3646	0.1080	11.83	2.30	3.33	13	8	33.0(1.4)	...	
08071+0509	0.0522	11.54	1.91	2.25	...	3	36.3(1.2)	C(1)	2
09320+6134	0.0394	11.72	2.15	1.61	12	7	170.9(5.9)	L(1),S2(2),L(4)	2,6
10038-3338	0.0341	11.40	1.71	2.92	315	6	24.7(1.6)	...	
10173+0829	0.0480	11.52	1.87	2.68	105	9	10.8(1.0)	...	
10378+1108	0.1362	12.02	2.57	3.27	13	8	8.9(0.6)	L(5,6)	
10485-1447	0.1330	11.90	2.40	2.91	...	2	4.4(0.6)	L(5)	2
11011+4107	0.0345	11.32	1.60	2.02	...	10	36.9(1.2)	C(1)	2,6
11069+2711	0.0703	11.50	1.85	24.8(1.2)	H/H(1)	1,2
11257+5850	0.0104	11.46	1.79	1.45	21	11	678.1(25.4)	C/H(1)	
11506-3851	0.0108	11.05	1.23	1.64	105	6	110.3(4.0)	...	
12018+1941	0.1687	12.13	2.72	2.87	3	12	6.5(0.5)	L(1)	
12112+0305	0.0730	12.08	2.65	2.96	45	6	23.8(0.9)	C,L(1,7)	
12243-0036	0.0073	10.79	0.88	0.04	7	12	41.4(1.3)	S2(1)	3
12540+5708	0.0422	12.13	2.72	2.87	50	11	309.9(12.1)	S1(1,7)	
13097-1531	0.0214	11.21	1.45	1.11	3	6	83.9(3.4)	H(1)	2,4
13126+2453	0.0112	10.78	0.85	0.27	...	13	31.2(1.0)	H(1)	2,3
13254+4754	0.0604	11.28	1.55	1.91	6	7	7.6(0.5)	C(1)	2
13428+5608	0.0378	11.87	2.36	2.55	70	11	145.4(5.2)	S2(1,7)	
13451+1232	0.1220	11.88	2.37	2.38	1.7	14	5398(162)	S1.5(1),S2(7)	
14070+0525	0.2644	12.50	3.23	4.40	10	15	5.2(0.5)	S2(7)	
15065-1107	0.0063	10.16	0.00	0.31	14	11	34.0(2.2)	S2(1)	3
15107+0724	0.0130	10.99	1.15	1.06	12.5	10	53.8(1.7)	H(1)	
15179+3956	0.0476	11.32	1.61	1.81	...	3	4.8(0.5)	H/H(1)	2
15233+0533	0.0541	11.41	1.73	12.7(0.6)	L(1)	1,2
15247-0945	0.0400	11.29	1.56	2.11	...	5	18.2(1.1)	L(1)	2
15250+3608	0.0554	11.71	2.14	2.58	...	16	14.9(0.6)	C(1),L(3)	2
15327+2340	0.0181	11.92	2.43	2.59	280	11	326.8(9.8)	S2(1),L(3,7)	
16145+4231	0.0231	10.37	0.28	1.84	...	2	10.3(0.6)	...	2,5
16399-0937	0.0270	11.20	1.44	1.69	25	17	57.9(2.2)	L/H(1)	2
17207-0014	0.0428	12.14	2.74	3.04	131	18	82.4(3.0)	L/L(1),H(7),L(8)	
17526+3253	0.0260	10.83	0.92	0.99	...	19	46.1(1.8)	H(1)	2
18544-3718	0.0734	11.61	0.734	2.00	42	6	5.6(0.6)	...	
20100-4156	0.1296	12.35	3.02	4.05	200	6	...	H(8)	
20491+1846	0.0290	10.84	0.94	1.07	...	3	24.1(1.1)	H(1)	2
20550+1655	0.0361	11.56	1.93	2.13	40	6	43.9(1.7)	H(1)	
22025+4204	0.0144	10.66	0.69	0.99	10	11	35.6(1.5)	C(1)	
22088-1831	0.1702	12.12	2.70	3.28	17	8	6.5(0.5)	H(5,8)	
22491-1808	0.0778	11.87	2.36	2.39	11	11	5.9(0.5)	H(3,4)	
23050+0359	0.0474	11.34	1.62	16.2(0.7)	H(1)	1,2
23135+2517	0.0273	11.21	1.45	0.79	2.4	9	35.5(1.5)	S2(1,3)	3
23365+3604	0.0645	11.86	2.34	2.45	...	2	28.7(1.2)	C(1),L(3)	2,6

^a1.4 GHz continuum fluxes are courtesy of the NRAO VLA Sky Survey (Condon *et al.* 1998).

^bSpectral classifications use the codes: “S1” = Seyfert 1; “S1.5” = Seyfert 1.5; “S2” = Seyfert 2; “L” = LINER; “H” = HII region (starburst); “A” = AGN; and “C” = Composite AGN and starburst.

REFERENCES.— OH line properties were obtained from: (1) Kazes, Mirabel, & Combes 1988; (2) Bottinelli *et al.* 1990; (3) Bottinelli *et al.* 1989; (4) Staveley-Smith *et al.* 1987; (5) Kazes, Mirabel, & Combes 1989; (6) Staveley-Smith *et al.* 1992; (7) Henkel & Wilson 1990; (8) Kazes & Baan 1991; (9) Mirabel & Sanders 1987; (10) Bottinelli *et al.* 1986; (11) Baan, Haschick, & Henkel 1992; (12) Martin *et al.* 1988; (13) Baan 1989; (14) Dickey *et al.* 1990; (15) Baan *et al.* 1992; (16) Bottinelli *et al.* 1987; (17) Staveley-Smith *et al.* 1986; (18) Bottinelli *et al.* 1985; (19) Kandalian 1996. Spectral classifications were obtained from: (1) Baan, Salzer, & LeWinter 1998; (2) Sanders *et al.* 1988; (3) Veilleux *et al.* 1995; (4) Smith, Lonsdale, & Lonsdale 1998; (5) Veilleux, Kim, & Sanders 1999; (6) Darling & Giovanelli 2002b (Paper V); (7) Kim, Veilleux, & Sanders 1998; (8) Duc, Mirabel, & Maza 1997.

NOTE.— (1) Listed as an OHM by Baan, Salzer, & LeWinter (1998), but no OH measurements exist in the literature; (2) No spectrum of this OHM is available in the literature; (3) OH kilomaser; (4) Baan, Salzer, & LeWinter (1998) measure $z = 0.0097$ for this object, which differs by 3900 km s^{-1} from the OH detection at $z = 0.0023$ (Henkel & Wilson 1990). Since the peak OH line is only 3 mJy, the validity of this OH detection is suspect; (5) Bottinelli *et al.* (1990) quote a distance of 375 Mpc in their detection announcement, but the luminosity distance derived from Grogin & Geller (2000) is a factor of four less, at 94 Mpc. Hence, this detection is probably spurious; (6) Baan, Haschick, & Henkel (1992) report upper limits on L_{OH} for this OHM which are significantly below published values, making the validity of this OHM suspect.

TABLE 9
PRINCIPAL COMPONENT ANALYSIS OF OHM AND HOST PROPERTIES.

Correlation Matrix						
	$\log(f_{100}/f_{60})$	$\log L_{60\mu m}$	$\log \Delta v$	$\log L_{OH}$	$\log L_{1.4GHz}$	
$\log(f_{100}/f_{60})$	1.00	-0.37	-0.10	-0.26	-0.14	
$\log L_{60\mu m}$		1.00	0.38	0.49	0.73	
$\log \Delta v$			1.00	0.65	0.52	
$\log L_{OH}$				1.00	0.63	
$\log L_{1.4GHz}$					1.00	
Mean	0.12	11.69	2.15	2.87	23.52	$N = 34$
Std. Dev.	0.13	0.29	0.36	0.53	0.32	
Eigenvectors						
	\hat{e}_1	\hat{e}_2	\hat{e}_3	\hat{e}_4	\hat{e}_5	Eigenvalues
	0.23	-0.48	-0.44	-0.50	-0.51	$\lambda_1 = 2.81$ (56%)
	0.87	-0.24	0.39	0.15	0.14	$\lambda_2 = 0.99$ (76%)
	0.36	0.53	-0.50	-0.36	0.45	$\lambda_3 = 0.67$ (89%)
	-0.05	0.28	0.63	-0.70	-0.15	$\lambda_4 = 0.33$ (96%)
	-0.25	-0.59	0.06	-0.32	0.70	$\lambda_5 = 0.20$ (100%)
RMS Residuals						
Principal Axis:	0.12	0.17	0.24	0.29	0.16	
Principal Plane:	0.04	0.15	0.20	0.27	0.16	
Princ. 3-Plane:	0.02	0.09	0.13	0.23	0.10	
Princ. 4-Plane:	0.01	0.08	0.01	0.07	0.10	
Princ. 5-Plane:	0.00	0.00	0.00	0.00	0.00	
Observation Errors						
	0.08	0.04	0.06	0.05	0.04	